UNIVERSIDADE Đ
COIMBRA

Fábio Alexandre Ferreira Henriques

DESIGN AND FABRICATION OF PHONON TRAPS TO REDUCE THE DENSITY OF QUASI -PARTICLES IN SUPERCONDUCTING QUANTUM CIRCUITS

Dissertação de Mestrado Integrado em Engenharia Física,
orientada pelo Doutor Ioan Pop e pelo Professor Doutor José António Paixão
e apresentada ao Departamento de Física da Faculdade de Ciências e Tecnologia
da Universidade de Coimbra

Setembro de 2018

Faculdade de Ciências e Tecnologias

DESIGN AND FABRICATION OF PHONON TRAPS TO REDUCE THE DENSITY OF QUASI-PARTICLES IN SUPERCONDUCTING QUANTUM CIRCUITS

Fábio Alexandre Ferreira Henriques

Dissertação no âmbito do Mestrado Integrado em Engenharia Física orientada pelo Doutor Ioan Pop[1] e pelo Professor Doutor José António Paixão e apresentada à Faculdade de Ciências e Tecnologias/Departamento de Física.

Setembro de 2018

---

[1] Physikalisches Institut, Karlsruhe Institute of Technology, 76131 Karlsruhe, Germany

UNIVERSIDADE Ð
COIMBRA

"Study hard what interests you the most in the most undisciplined, irreverent and original manner possible."

Richard Feynman

UNIVERSITY OF COIMBRA

Abstract

Faculty of Science and Technology
Physics Department

Master in Engineering Physics

Design and fabrication of phonon traps to reduce the density of quasiparticles in superconducting quantum circuits.

by Fábio HENRIQUES

English

Superconducting quantum circuits are an active field of research with various applications such as quantum computation and radiation detection. These circuits are made of thin films of superconducting materials deposited over a dielectric substrate, and their efficiency can be degraded by the presence of quasi-particles. In this text we propose, that phonon propagation in the substrate can act as a mediator for the creation of quasi-particles, and we introduce a strategy to suppress this phenomena by implementing phonon traps. We tested the effects of Aluminum phonon traps in granular Aluminum resonators and measured an increase of internal quality factor in the single photon regime of up to a factor of 3. We also observed a partial suppression of $1/f$ noise and of rate and energy of stochastic bursts, indicating that quasi-particle creation is partially mediated by phonon propagation in the substrate, and that the implementation of phonon traps can improve their performance.

Keywords: phonon traps, superconducting circuits, granular Aluminum, resonators, quasi-particles

Português

Circuitos supercondutores quânticos oferecem um leque abrangente de aplicações em campos como computação quântica e detecção de radiação. Estes circuitos são compostos por filmes finos de materiais supercondutores depositados sobre um substrato dieléctrico, e a sua eficiência pode ser prejudicada pela presença de quase-partículas. Neste texto propomos que a propagação de fonões no substrato pode actuar como mediador para a criação destas partículas. Introduzimos também uma estratégia para suprimir este fenómeno, implementando traps de fonões. Testamos os efeitos de armadilhas de fonões feitas de Alumínio em ressonadores de Alumínio granulado. E medimos um aumento no factor de qualidade interno de 3 vezes. Observamos também a supressão parcial do ruído $1/f$ e da taxa e energia de eventos. Indicando que a criação de quase-partículas é de facto mediada pela propagação de fonões, e que a implementação de traps de fonões pode de facto melhorar o desempenho de circuitos supercondutores quânticos.

Palavras-chave: armadilhas de fonões, circuitos supercondutores, Aluminio granulado, ressonadores, quase-partículas

Acknowledgements

I would like to thank my parents for all the sacrifices they made in order to allow me and my siblings to study, I will forever owe them everything I'll accomplish. *Gostaria de agradecer aos meus pais por todos os sacrificios que fizeram para que eu e os meus irmãos pudessemos estudar, devo-lhes tudo o que alguma vez alcançar.*

I would also like to thank my brother and my uncle Manuel who gave me the best advice I could ever hope for.

Thank you to my class mates and friends with whom I spent the most fun and rewarding years of my life during university. Emanuel, Catarina, Guerreiro, Tiago, Oliveira, Antunes, António, freshman João, Queiroz and everyone else, Thank You!

Thank you to everyone with whom I lived in the Santos Rocha residency, you guys are awesome.

Thank you as well to everyone who helped me through out my stay in Germany, I couldn't have done it with out them. A very special thanks to Francesco in particular, who kept me sane during the work for my thesis.

Thank you to Erasmus, It was financed my stay in Germany and without it I would never had been able to do it.

Finally, to Dr Ioan Pop, the person who accepted me with open arms in his group and allowed me to do something that I really loved, who trusted me, who changed my life for the best. I'm not sure if thank you is enough.

Contents

List of Figures

List of Tables

Chapter 1

Introduction

Superconducting quantum circuits are more than ever an active field of research. Made of thin superconducting films deposited over a dielectric substrate, these electrical circuits allow for the observation of quantum phenomena at a macroscopic scale. This promising technology has a wide range of applications such as radiation detection in the form of kinetic inductance detectors (KID's)[1], extremely sensitive magnetometers as superconducting quantum interference devices (SQUID's)[2] and single Cooper pair transistors[3]. Most importantly is the role of these circuits as a candidate for the physical implementation of fault tolerant quantum computation, with superconducting qubits showing coherence times in the order of tenths of microseconds[4] and reliable gate performance[5], while being easy to fabricate and presumably scalable[6]. Although fault tolerant quantum computing is still not a reality, other quantum information devices based on superconducting circuits have already found applications in the forms of quantum annealing[7] and quantum simulation[8].

Even though these circuits have been shown to be reliable in their many applications, there still is a long way to go in improving their performance. Especially in superconducting qubits, a great effort has been put forward by the community to improve coherence times and noise performance, which have been shown to be limited by factors such as dielectric loss[9], two level system (TLS) defects in the substrate[10], magnetic spins in the surface of the dielectric[11] and the subject of this work, quasi-particles (QP).

The presence of quasi-particles in the circuits introduces a channel for dissipation and can add noise. Theory predicts that at low temperatures ($\approx 20\,\mathrm{mK}$) superconducting Aluminum in thermal equilibrium should not have more than one quasi-particle in the volume of earth. However, this is not the case, as a substantial background of QP can be observed in most superconducting circuits[12, 13, 14]. It is thus important to study the generation and relaxation mechanisms of quasi-particle in order to suppress them. Sources of QP have been linked mostly to pair-breaking stray radiation[15], but it is still unknown if there are any other sources[16]. Strategies already exist to lower the number of QP, like shielding from exterior radiation[17], metal quasi-particle traps[18], and Abrikosov vortex trapping [12].

In this project we introduce Phonon Trapping as a new method to limit the quasi-particles density. It has been shown that phonons populating the substrate can create QP. Thus, eliminating phonon propagation could effectively lower the QP density (in the case of this mechanism being a dominant source of QP, which is not obvious). Furthermore, it is known that external radiation can create phonons in the substrate, this phenomena can even be used for particle detection in phonon mediated kinetic inductance detectors[19, 20]. Given that typically the circuits occupy a small fraction of the substrate's surface, it would be reasonable to assume that quasi-particle generation from external radiation is mostly mediated by phonon propagation.

In this context, phonon traps consist of a second superconducting film with lower gap, deposited on the substrate alongside the circuit. They act as phonon absorbers, decreasing phonon propagation in the dielectric[1]. In order to test their effectiveness and subsequently the relevance of phonon propagation in superconducting circuits, we test the influence of Aluminum traps in granular Aluminum superconducting resonators. Granular Aluminum is a great material for the study of QP dynamics as its high kinetic inductance makes resonators made out of it highly sensitive to quasi-particles. We study phonon propagation and trapping by having several samples with different area of the substrate covered in traps and comparing the loss and noise performance in each of the resonators.

This thesis is organized as follows:

In chapter 2 we will talk about the necessary theoretical concepts needed to understand the experiments. Sections 2.1 and 2.2 contain generalized textbook physics concepts. Namely on microwave engineering and superconductivity, based mostly on [21] and [22] respectively; the experienced reader can skip these sections. Section 2.3 is about superconducting resonators, section 2.2.3 is specifically about granular aluminum. Finally, in section 2.4 we present the details on phonon propagation and phonon trapping.

Chapter 3 contains a detailed description of the experimental methods used during the project, as follows: sample design in section 3.1, fabrication process in section 3.2, sample mounting 3.3 and measurement setup used to take the data in section 3.4.

The results are presented and discussed in chapter 4, where the three main figures of merit are shown: dissipation performance in section 4.2, noise performance in 4.3, and the effects of phonon traps on stochastic bursts in section 4.4.

---

[1] The mechanism is explain in detail in section 2.4

Chapter 2

Theory

2.1 Microwave Domain

In most electronic applications the wavelengths of voltage and current waves are orders of magnitude larger then the physical size of the circuit. This enables the use of Lumped element model (LEM) when describing them. In LEM an electric circuit is composed of discrete elements connected by shorts. This approximation is reasonable because there are no major fluctuations of phase and amplitude along the length of the cables. When in the microwave regime (300 MHz to 300 GHz), wavelengths in the range of $\lambda = c/f = 1\,\mathrm{m}$ to $1\,\mathrm{mm}$ are comparable to the dimensions of the circuits. In this case LEM is no longer a viable approximation and has to be replaced by the distributed element model (DEM). A detailed description of this model and other microwave properties can be found in [21], which was used extensively in the writing of this chapter.

2.1.1 Transmission Line

In DEM simple wires connecting elements are replaced by transmission lines, whose representation is shown in figure 2.1. A transmission line is composed of two conductors separated by a dielectric medium. The DEM representation of a transmission line takes into account four effects: electrical losses due to the resistivity of the wire R, the self inductance L, capacitance between the two wires C, and losses in the dielectric medium G. All these per unit of length.

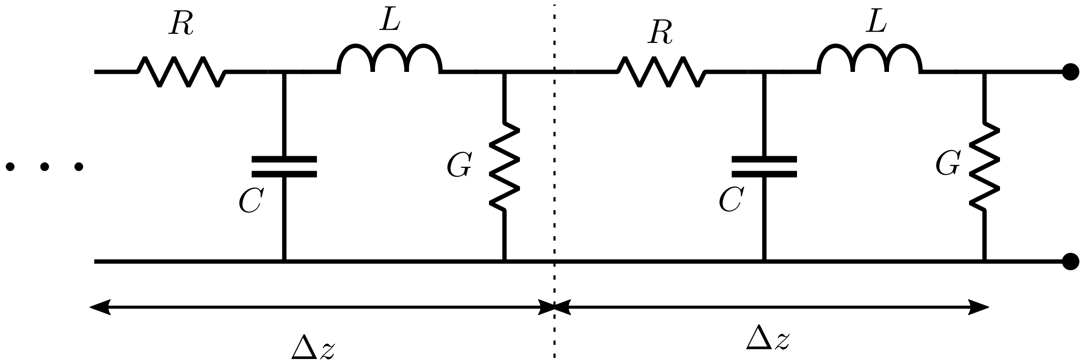

FIGURE 2.1: Representation of a transmission line with the four effects R, C, L and G.

This allows us to write the so called *telegraph equations* in the limit of $\Delta z \to 0$ in phaser notation:

$$\mathrm{d}_z V(z) = -(R + j\omega L)I(z) \tag{2.0a}$$
$$\mathrm{d}_z I(z) = -(G + j\omega C)V(z) \tag{2.0b}$$

Joining both equations we are able to write the separate equations for voltage and current:

$$\mathrm{d}_z^2 V(z) - \gamma^2 V(z) = 0 \tag{2.1a}$$
$$\mathrm{d}_z^2 I(z) - \gamma^2 I(z) = 0 \tag{2.1b}$$

Where $\gamma = \alpha + j\beta = \sqrt{(R + jwL)(G + jwC)}$. The real part α quantifies the loss in the transmission line while the imaginary part is the wave number $\beta = {}^{2\pi}/_{\lambda}$. The solutions of equations 2.1 take the form:

$$V(z) = V_0^+ e^{-\gamma z} + V_0^- e^{\gamma z} \tag{2.2a}$$
$$I(z) = I_0^+ e^{-\gamma z} + I_0^- e^{\gamma z} \tag{2.2b}$$

Where $+$ and $-$ represent propagation in the positive and negative z directions respectively. We introduce as well the intrinsic impedance of the circuit Z_0 as the ratio between voltage and current. It is an intrinsic property of the transmission line dependent on its geometry and material.

$$Z_0 = \frac{V_0^+}{I_0^+} = -\frac{V_0^-}{I_0^-} = \sqrt{\frac{R + j\omega L}{G + j\omega C}} \tag{2.3}$$

In most applications dissipation can be disregarded, and we obtain the impedance $Z_0 = \sqrt{{}^{L}/_{C}}$ and $\gamma = j\beta = j\omega\sqrt{CL}$. In summary a transmission line can be described by three distinct quantities, Z_0, β and α which are all intrinsic properties.

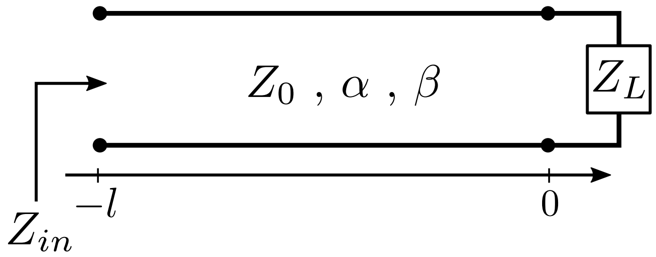

FIGURE 2.2: Scheme of a loaded transmission line with parameters Z_0, α, β and load Z_L.

By adding a load Z_L to the transmission line, as represented in figure 2.2, part of the incoming waves will be reflected at the load while the rest is absorbed. In order to quantify this effect we introduce the concept of reflection coefficient, defined as the fraction of reflected voltage at the load ($z = 0$):

$$\Gamma = \frac{V_0^-}{V_0^+} = \frac{Z_L - Z_0}{Z_L + Z_0} \tag{2.4}$$

From equation 2.4 it is seen that when the load impedance is equal to the intrinsic impedance of the line the reflection coefficient is zero, hence there are no reflecting waves. In this case we call the load *matched* ($Z_L = Z_0$). The standard for transmission line impedance is 50 Ω, and in order to avoid unwanted reflection most components have to be matched to this value.

The last concept we have to introduce is the input impedance of a loaded transmission line shown in figure 2.2 as Z_{in}. In order to get an expression for it we must first rewrite equations 2.2 using the reflection coefficient.

$$V(z) = V_0^+ \left(e^{-j\beta z} + \Gamma e^{j\beta z}\right) \tag{2.5a}$$

$$I(z) = \frac{V_0^+}{Z_0} \left(e^{-j\beta z} - \Gamma e^{j\beta z}\right) \tag{2.5b}$$

With this we use the same concept of equation 2.3 to get the input impedance.

$$Z_{in} = \frac{V(-l)}{I(-l)} = \frac{1 + \Gamma e^{-2j\beta l}}{1 - \Gamma e^{-2j\beta l}} Z_0 = Z_0 \frac{Z_L + jZ_0 \tan \beta l}{Z_0 + jZ_L \tan \beta l} \tag{2.6}$$

This is a rather important result since we have the total impedance of a loaded transmission line as a function of the circuit parameters and it will be useful in next section's discussion.

2.1.2 Open-Ended $\lambda/2$ Resonator

The main circuit element used in this work is the open-ended $\lambda/2$ resonator, in this case in the form of strip-lines. These resonators are equivalent to parallel RLC circuit for which the impedance is given by:

$$Z_{RLC} = \left(\frac{1}{R} + \frac{1}{j\omega L} + j\omega C\right)^{-1} \tag{2.7}$$

Such resonator is in resonance when the electrical energy stored in the capacitor $W_e = \frac{1}{4}|V|^2 C$ is equal to the magnetic energy stored in the inductor $W_m = \frac{1}{4}|I|^2 L$ which happens at the resonance frequency ω_0.

$$\omega_0 = \frac{1}{\sqrt{LC}} \tag{2.8}$$

We can rewrite equation 2.7 by letting $\omega = \omega_0 + \delta\omega$, where $\delta\omega$ is small, and by making use of the approximation $\frac{1}{x+1} \approx 1 - x$.

$$Z_{RLC} \approx \frac{R}{1 + 2j\delta\omega RC} \tag{2.9}$$

And since $\omega_0^2 = 1/LC$ and for low loss resonators ($R \to \infty$) we can write:

$$Z_{RLC} \approx \frac{1}{2jC(\omega - \omega_0)} \tag{2.10}$$

Another important quantity to introduce is the internal quality factor defined as the ratio between average energy stored and energy lost in the resonator:

$$Q_i = \omega \frac{\text{average energy stored}}{\text{energy loss per unit of time}} = \omega_0 \frac{W_m + W_e}{P_l} \tag{2.11}$$

Where $P_l = \frac{1}{2}\frac{|V|^2}{R}$ is the power loss. With this quantities defined, and knowing that at resonance $W_m = W_e$ we can rewrite the quality factor at resonance as:

$$Q = \frac{\omega_0 L}{R} = \frac{1}{\omega_0 RC} \tag{2.12}$$

Now that we defined the impedance and quality factor of a typical RLC parallel resonator we can make the leap to $\lambda/2$ resonators. A $\lambda/2$ resonator is nothing more than a transmission line with length l shown in figure 2.3 where the load is an open circuit ($Z_L \to \infty$). Resonance occurs when incoming and reflected waves interact constructively creating standing waves. Their mathematical description begins with the lossy version of equation 2.6 for an open circuit as load.

$$Z_{in} = Z_0 \coth(\alpha + j\beta)l = Z_0 \frac{1 + j\tan\beta l \tanh\alpha l}{\tanh\alpha l + j\tan\beta l} \tag{2.13}$$

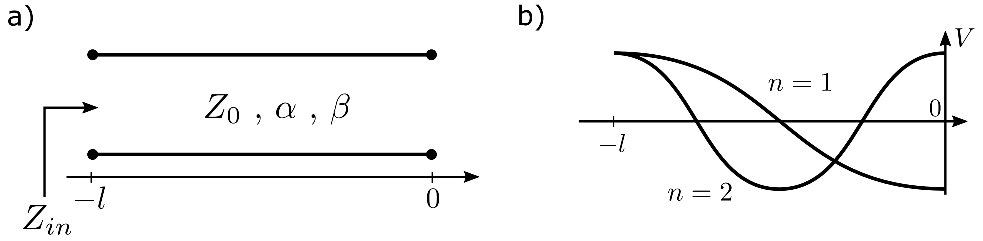

FIGURE 2.3: (a) Scheme of an open circuited $\lambda/2$ resonator. (b) Representation of the first two resonant modes ($n = 1$ and $n = 2$) in voltage.

At resonance ($\omega = \omega_0$) the length of the line is equal/multiple of half the wavelength ($l = \lambda/2$). Introducing once again $\omega = \omega_0 + \delta\omega$, we can write $\beta l = \pi + \frac{\pi\delta\omega}{\omega_0}$. For frequencies near resonance we have $\tan\beta l = \tan\frac{\pi\delta\omega}{\omega_0} \approx \frac{\pi\delta\omega}{\omega_0}$. And for low loss resonators making the approximation $\tanh\alpha l \approx \alpha l$ we can rewrite equation 2.13:

$$Z_{in} = \frac{Z_0}{\alpha l + j(\pi\delta\omega/\omega_0)} \tag{2.14}$$

Comparing it to the impedance of a parallel RLC resonator described in equation 2.10 we extract the equivalent resistance, capacitance and inductance, established the relation between a $\lambda/2$ resonator and a traditional parallel RLC resonator.

$$R = \frac{Z_0}{\alpha l} \tag{2.15a}$$

$$C = \frac{\pi}{2\omega_0 Z_0} \tag{2.15b}$$

$$L = \frac{1}{\omega_0^2 C} \tag{2.15c}$$

In order to excite the resonator it is required to couple it to exterior circuits. This is done by coupling it to a transmission line through a coupling transformation, and reading out the signal with the appropriate electronics as depicted in figure 2.4.

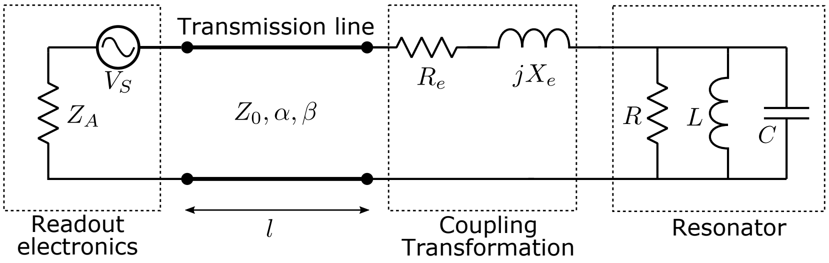

FIGURE 2.4: Coupling scheme between the resonator and the readout set up. Figure adapted from [23]

The total system (resonator plus coupling) will have different reflection properties than the resonator by itself. Seen from the point of view of the readout electronics, the input signal can either be reflected or absorbed by the resonator. As such we define the coupling quality factor Q_c, as the ratio of power that gets absorbed by the resonator. Higher Q_c meaning worse coupling and vice-versa. We can thus define the total (or loaded) quality factor Q_l of the system:

$$\frac{1}{Q_l} = \frac{1}{Q_i} + \frac{1}{Q_c} \tag{2.16}$$

The resonant frequency will also change but not significantly, $f_{0L} \approx f_0$. Using equation 2.4 to the circuit of figure 2.4 following the method described in detail in [23] we are able to demonstrate the typical reflection coefficient for this system:

$$\Gamma = \Gamma_d \left[\frac{\frac{Q_c - Q_i}{Q_c + Q_i} + 2jQ_l\delta\omega/\omega_0}{1 + j2Q_l\delta\omega/\omega_0} \right] \tag{2.17}$$

Where Γ_d is the detuned reflection coefficient far from resonance. By fitting the reflection results, it is possible to distinguish between the two coupling factors Q_i and Q_c, which is important because the main figure of merit is the internal Q. The general shape of the reflection coefficient can be seen in figure 2.5.

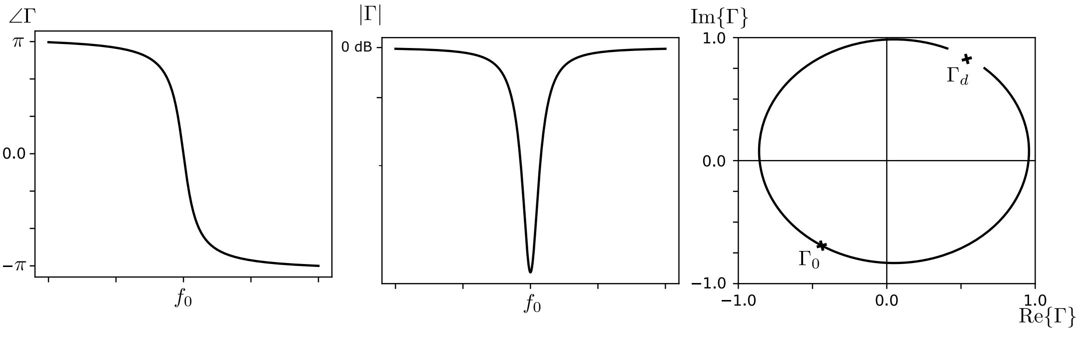

FIGURE 2.5: (left) Typical phase response of a resonator. (center) amplitude response. (right) Complex plain representation of the Q circle . Every plot for $Q_i > Q_c$.

The phase response of a typical resonator follows the shape of an arctan, which coincides with a 2π roll-off with the resonant frequency being in the center of it. The amplitude is characterized by a dip with minimum at resonance. The dip width and depth are characterized by the quality factors. Lastly, the complex plain of these reflection takes the form of a circle. Dissipation can be seen in the circle in proximity of the resonance point Γ_0 to the center of the plain.

Furthermore, by knowing the internal and coupling quality factors, it is possible to estimate the average number of photons populating the resonator $\bar{n}$. Let P_{in} be the input the power, P_{abs} the power absorbed by the resonator, and P_{ref} the reflected power. As the input power can either be reflected or absorbed by the resonator we have $P_{in} = P_{ref} + P_{abs}$, and by definition:

$$\Gamma^2 = \frac{P_{ref}}{P_{in}} = 1 - \frac{P_{abs}}{P_{in}} \tag{2.18}$$

Note that reflection parameter is squared because it is defined with voltage as in equation 2.4, and we are working with powers. Close to resonance it is demonstrated in[24] that:

$$\Gamma = Q_L \left(\frac{1}{Q_i} - \frac{1}{Q_c} \right) \tag{2.19}$$

Squaring equation 2.19, and using equation 2.16 we get:

$$\Gamma^2 = 1 - 4\frac{Q_L^2}{Q_i Q_c} = 1 - \frac{P_{abs}}{P_{in}} \tag{2.20}$$

The energy of a photon in the resonator is given by $\hbar\omega_0$, and thus the total energy stored in the resonator at a given moment is given by the number of photons $\bar{n}$ times the energy per photon. We can then rewrite equation 2.11:

$$Q_i = \omega_0 \frac{\bar{n}\hbar\omega_0}{P_{abs}} \tag{2.21}$$

And finally:

$$\bar{n} = 4\frac{P_{in} Q_l^2}{Q_c \hbar \omega_0^2} \tag{2.22}$$

2.2 Superconductivity

Discovered in 1911 by the Dutch physicist Heikke Onnes, superconductivity is a phenomenon characterized by zero DC resistivity and the total expulsion of magnetic field in the interior of the material, also known as Meissner effect, when cooled to temperatures lower than a certain critical temperature Tc. The microscopic properties of superconductivity are a quantum phenomena described by the Bardeen-Cooper-Schrieffer (BCS) theory[25]. However some macroscopic properties can be approximately described by purely classical models. In this section we will firstly describe a few general electrical properties of superconductors giving use to the two fluid model. Lastly, we will give a small introduction into some of the more important microscopic properties of superconductivity using the BCS theory. For a more detail description, see[22].

2.2.1 Electrical Properties

In the two fluid model, it is considered that the current is carried by two distinct charge carriers: particles with superconducting properties called Cooper pairs (CP) and normal particles called quasi-particles (QP), with densities n_s and n_n respectively [1]. They differ from each other because unlike CP, QP dissipate when traveling through the superconductor.

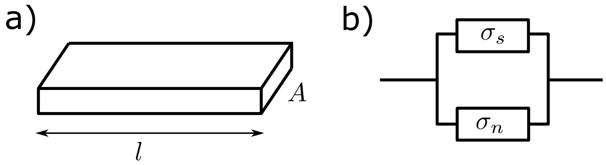

FIGURE 2.6: Electrical scheme of the two fluid model (a) a bar of length l and cross section are A of superconducting materials behaves similarly to (b) two parallel impedances $l/A\sigma_n$ and $l/A\sigma_s$.

A superconducting wire, as shown in figure 2.6 a) can be modeled as a parallel circuit consisted of two channels, one for QP with conductivity σ_n and the other for CP with conductivity σ_s, as shown in b) of the same figure.

The conductivities of each channel are given in a simplified way by the Drude model. It assumes that charge carriers in a metal loose energy through impacts with the ion lattice. The average time between impacts is given by τ_i, where i in the two fluid model can be either s or n, referring to CP and QP. The Drude model predicts an AC conductivity given by:

$$\sigma_i = \sigma_{1i} - j\sigma_{2i} = \frac{\sigma_{0i}}{1+\omega^2\tau_i^2} - j\frac{\sigma_{0i}\omega\tau_i}{1+\omega^2\tau_i^2} \tag{2.23}$$

Where $\sigma_{0i} = n_i q_i^2 \tau_i / m_i$ is the DC conductivity of the material and q_i is the charge and m_i the mass of the charge carriers. As we are using the conductivity of two parallel channels, the total conductivity will be the sum of both. That leaves us with four terms in the total conductivity, σ_{1s}, σ_{2s}, σ_{1n} and σ_{2n}. As CP can move without dissipation we take the limit $\tau_s \to \infty$. In this case σ_{1s} is only different from zero for $\omega = 0$ where it diverges, meaning conduction with no dissipation while σ_{2s} takes the form $n_s q_s^2/m\omega$. In most metals and conventional superconductors τ_n is in the order of 10^{-14}s and this formula is only applicable for frequencies lower than the superconducting gap, thus σ_{2n} is negligible for the frequencies used in this project. We can thus write the total conductivity:

$$\sigma = \frac{\pi n_s q_s^2}{2m_s}\delta(\omega) + \frac{n_n q_n^2 \tau_n}{m_n} - j\frac{n_s q_s^2}{m\omega} \tag{2.24}$$

The real component of equation 2.24, which quantifies dissipation, is composed of a term dependent on the density of CP that vanishes in the AC regime, and another term which depends on the density of QP that accounts for dissipation due to the presence of QP. The imaginary component depends only on the density of CP and it arises from the fact that CP cannot respond instantaneously to an applied electrical field due to their inertia and it is proportional to the inverse of the frequency, behaving as an inductance. If we consider a superconducting wire with cross-section A and length l we can define the kinetic inductance L_k from this term as:

$$L_K = \frac{l}{A\omega\sigma_2} = \frac{lm}{An_s q^2} \tag{2.25}$$

---

[1] in section 2.2.2 we will go into further detail in the their description

In a different way comparing the the kinetic inductance stored in the CPs to an inductor with the same current we achieve the same result in a different way:

$$\frac{1}{2}n_s lAm\left(\frac{J}{n_s q}\right)^2 = \frac{1}{2}L_K(JA)^2 \Rightarrow L_K = \frac{lm}{An_s q^2} \tag{2.26}$$

The dependency of the kinetic inductance on the density of Cooper pairs is what will allow us to study the quasi-particle dynamics, as we will see in section 2.3.

2.2.2 Microscopic Properties

In the last section we introduced the concepts of Cooper pairs and quasi-particles without describing any of their microscopic properties. In this section, we will describe some of their fundamental properties giving use to the Bardeen Cooper Shrieffer theory. And also introduce a few key concepts of the BCS theory.

In 1956 in an effort to discover a microscopic description of superconductivity, Leon Cooper proved that in the presence of an arbitrarily small attractive interaction between two electrons, it is possible to have a bound state with energy below the Fermi level. We call the bound state a Cooper pair. In conventional superconductors the bounding has been proven to be due to phonon-electron interaction. Once in the bound state the composite pairs can create a condensate. One can demonstrate that once there is pairing, a gap is created in the energy distribution of electrons equal to the energy necessary to separate the electrons of Cooper pairs. This is called the superconducting gap, Δ. With a gap in the distribution of energy levels, the condensate cannot win or loose energy by amounts below Δ. Hence phenomena like scattering are not allowed and the condensate can flow freely without dissipation.

If a Cooper pair is excited and leaves the condensate it gives rise to two electron like excitations. These excitations behave mostly like electrons but have some fundamental differences that make us rename them as quasi-particles. As charged particles they take part in the conduction of current but are susceptible to dissipation.

BCS theory also provides some insight into the conduction properties of superconductors. Most importantly it gives quantitative values for the imaginary component of equation 2.24:

$$\frac{\sigma_2}{\sigma_n} = \frac{\pi\Delta(T)}{hf}\tanh\frac{\Delta(T)}{2k_BT_c} \tag{2.27}$$

Where σ_n is the normal state conductivity of the material. By assuming the BCS gap ($\Delta(0) = 1.76\pi k_BT_c$) and $T \ll T_c$ equation 2.27 simplifies to:

$$L_k = 0.18\frac{\hbar}{k_BT_c}R \tag{2.28}$$

Where R is the room temperature resistance. This expression allows us to predict L_k by measuring the room temperature resistance of the superconductor.

2.2.3 Granular Aluminum

Granular Aluminum (*grAl*) is a granular superconducting material composed of an assemble of 2-4 nm diameter pure aluminum (*Al*) grains distributed on an aluminum oxide matrix (AlO_x)[26, 27, 28], as shown in figure 2.7. It is fabricated by evaporating pure aluminum in an oxygen atmosphere. Changing the oxygen partial pressure during evaporation allows to tune the room temperature resistivity of the films, reaching values between 1 and $10^5\,\mu\Omega\,\mathrm{cm}$. The critical temperature increases with ρ reaching a maximum of $2.2\,\mathrm{K}$ at $\rho \approx 4 \times 10^2\,\mu\Omega\,\mathrm{cm}$[29], then decreases until the superconducting to insulator transition. From equation 2.28 we also see that the kinetic inductance can be tuned with this method reaching values in the order of nH/sq for high resistive films.

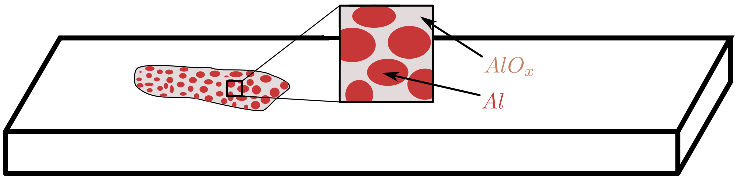

FIGURE 2.7: A film of granular aluminum is represented. In gray aluminum oxide and in red the grains of pure aluminum. Figure adapted from *Maleva, et al* [30]

It is a material of interest because it allows for low-loss high kinetic inductance environments enabling for highly compact microwave resonator structures. The high kinetic inductance, how we see in equation 2.31, makes superconducting resonators more sensible to the presence of QP.

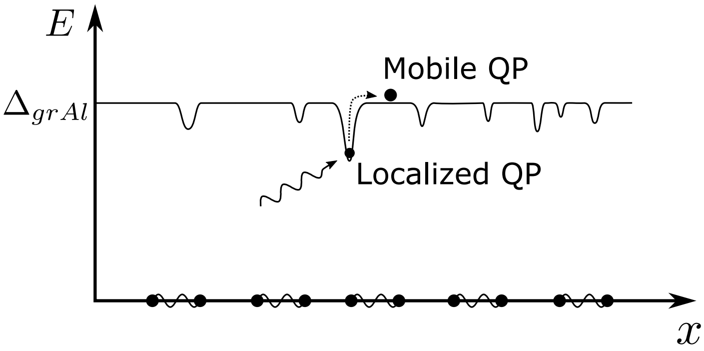

FIGURE 2.8: Toy representation of the spatial distribution of the lower energy quasi-particle state. In $grAl$ there are regions where the minimum energy state for quasi-particles is lower then the gap, as demonstrated in [31]. Here we show an example of how this minimum energy state might vary along $grAl$, representing localized and mobile quasi-particles and an excitation.

The microscopic structure of $grAl$ suggests that there are spatial variation of the quasi-particle density of states as described in [31]. Giving rise to local minimums where QP can stay trapped, as shown in figure 2.8. We denote these QPs localized and higher energy QP that can move through the material, we call mobile. In *Grunhaupt et al.* these concepts where used to formulate a model where localized QP can be excited, for example by phonons, to higher energy states and become mobile. Mobile QP can recombine more easily because it is easier for them to find other QP.

2.3 Superconducting resonators

Superconducting resonators follow the same functioning principles as normal microwave resonators described in section 2.1.2, with the added effect that dissipation is much lower due to the low AC resistivity, enabling the observation of quantum phenomena, mainly discretized energy levels similar to the harmonic oscillator.

Specifically for superconducting resonators, dissipation as been shown to be dominated by factors such as dielectric loss [32], the presence of spins in the surface of the dielectric [33], and quasi-particles[34]. In this work we are mainly interested in quasi-particle dissipation. It arises from equation 2.24 that QP add a resistive element to the system and lower the internal quality factor.

Besides Q_i, QP also have an influence on the resonance frequency seen that it depends on kinetic inductance which depends on the number of QP in resonator:

$$f_0 = \frac{1}{2\pi\sqrt{(L_G + L_k)C}} \tag{2.29}$$

where L_G is the geometric inductance and only depends on the geometry of the resonator, as does the capacitance C. Defining the kinetic inductance fraction $\alpha = L_k/(L_k + L_G)$ and using equation 2.29 we can write:

$$\frac{\delta f_0}{f_0} = -\frac{\alpha}{2}\frac{\delta L_K}{L_K} \tag{2.30}$$

meaning that a shift in kinetic inductance by breaking or creating cooper pairs causes a shift in resonance frequency. One can even extend this using equation 2.25 and write:

$$\frac{\delta f_0}{f_0} = -\frac{\alpha}{2}\delta x_{qp} \tag{2.31}$$

where x_{qp} is the normalized density of quasi-particles. This makes superconducting resonators a great tool in the study of QP dynamics in superconductor in general, and is the operational basis for kinetic inductance detectors.

The BCS theory gives a prediction for the quasi particle density as a function of temperature. By plugging this dependency into equation 2.31 we see that resonance frequency goes down with temperature as given by:

$$\frac{\delta f_0(T)}{f_0(0)} = -\frac{\alpha}{2}\sqrt{\frac{\pi\Delta}{2k_BT}}\exp\left(-\frac{\Delta}{k_BT}\right) \tag{2.32}$$

By measuring the resonant frequency vs temperature, and fitting equation 2.32, we are able to extract the kinetic inductance fraction and the superconducting gap of the resonator.

2.4 Phonon Trapping

As stated in the introduction, in most superconducting circuits there is a surplus of quasi-particles, for which the source is unknown. We propose that phonon propagation in the substrate can serve as mediator for external radiation to break cooper pairs and create this excess. If one is able to efficiently absorb phonons before they reach the circuit, the density of quasi-particles will be lower. In order to trap the phonons, we implement phonon traps, which are a second superconducting material deposited alongside the circuit. In this project, the circuit of interest are superconducting resonators made of *grAl* while the traps are made of Aluminum. We chose these materials because in order for the traps to be efficient they need lower superconducting gap.

Consider a *grAl* superconducting film, deposited on a substrate where phonons can propagate. When these phonons reach the film, if they have enough energy ($h\nu > \Delta_G$) they will create QP that will eventually recombine and send a phonon back to the substrate. This will create a vicious cycle where phonons create QP and QP create phonons. The cycle would eventually end because phonon would loose energy due to scattering. However, as we consider that there is an exterior source which creates phonons with a rate g_P the system will reach a stable state instead. The density of QP in this steady state will be higher than the case without phonon propagation.

By adding a second superconductor with lower gap, in this case *Al*, part of the phonons will be absorbed by it instead. As the density of states for QP in superconductors is higher at energies closer to the gap, the QP will tend to populate these states. They will loose the energy necessary to reach them by scattering, emitting low energy phonons into the substrate. The phonons created by the recombination in *Al* will then have energy close to the *Al* gap, which is not enough to break CP in *grAl*, effectively removing them from the system.

An empiric model for this process was developed by *Valenti et al.*[35] which we present in the next paragraphs. Consider that after being generated, phonons quickly reach a steady state and can be collectively described by a single distribution. Moreover since the system is at low temperatures ($k_bT \ll \Delta_G, \Delta_A, \Delta_G - \Delta_A$) we neglect the effects of any thermal phonons, and consider only "hot" phonons with energy above the highest *grAl* gap ($E_P > \Delta_G^{max}$), in order to consider the Cooper pair breaking rate independent of spatial distribution.

We indicate N_A and N_G as the number of quasi-particles in Aluminum and *grAl* films respectively, and N_P as the number of phonons in the system.

We model the quasi-particle and phonon dynamics in a phenomenological way, with rate equations of the Rothwarf-Taylor type [36]. For quasi-particles in *grAl* the relevant processes are the generation by pair breaking from hot phonons (rate b_G) and recombination (rate r_G). Similarly, in *Al* we have generations and recombination (rates b_G and r_A), but also scattering of QP to lower energies (rate s_A) with emission of lower energy phonons not capable of breaking cooper pairs in *grAl*. For the phonons, we assume an unknown generation mechanism with rate g_P, in addition to the generation/recombination in *grAl* and *Al*. The rate equations are then:

$$\dot{N_G} = -2r_G N_G^2 + 2b_G N_P \tag{2.33}$$

$$\dot{N_A} = -2r_A N_A^2 + 2b_A N_P - s_A N_A \tag{2.34}$$

$$\dot{N_P} = g_P - b_A N_P + 2r_A N_A^2 - 2b_G N_P + r_G N_G^2 \tag{2.35}$$

Note that there are some effects not considered in this model. Mainly the phonons

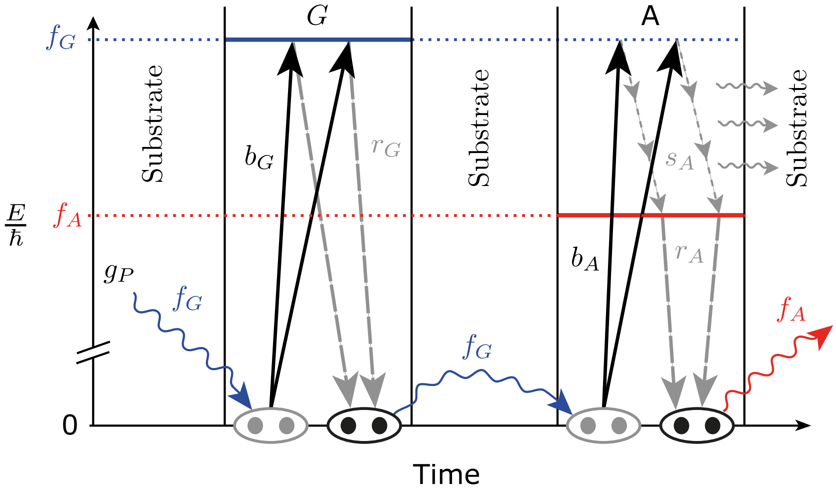

FIGURE 2.9: Representation of phonon propagation and phonon trapping in superconducting circuits. The y axis shows an energy scale in frequency units, the y axis shows time. In blue is represented the gap of $grAl$ and in red the gap of Al. From left to right we have substrate, $grAl$ film, substrate, Aluminum film and substrate again. Phonons are created at the substrate at a rate g_p. Cooper pairs are broken and recombine in $grAl$ with rates b_G and r_G respectively. Recombination in $grAl$ creates a phonon with energy approximately f_G that travel to the Al film where it breaks CP with a rate b_A creating QP that recombine at a rate r_A and scatter at a rate s_A, releasing low energy photons to the substrate. A phonon is emitted to the substrate with energy approximately f_A. Figure adapted from *Valenti et al*[35].

can escape the substrate to the sample holder, in the same way phonons from the sample holder can travel to the substrate, but both this effects don't depend on the number of phonons and hence can be considered to be integrated in g_P. We have also neglected phonon scattering that cools them below the $grAl$ gap, this would add a term $-s_P N_P$ to equation 2.35, but it can be neglected.

The effectiveness of phonon trapping is partially determined by the scattering of QP in Al (with rate s_A) that effectively reduces the total number of high energy QP in Al and consequentially the number of high energy phonons populating the substrate. By changing the difference between the gaps we are effectively increasing this rate. Another quantity of importance is the generation rate in Al (b_A) the higher it is, the more QPs available to scatter and eliminate phonons. It can be increased by increasing the area and the thickness [20] of the traps. In conclusion we expect the traps to be more efficient, the thicker they are, the more area they cover and the higher the gap difference between Al and $grAl$.

Chapter 3

Methods

3.1 Design

We use superconducting resonators as a mean to study the effects of phonon trapping in superconducting circuits. The resonators chosen should have a design and material such that loss and noise are dominated by quasi-particles rather than any other source. The resonators used by *Grunhaupt et al.*[37] satisfy this requirements and we will use the same design.

We chose 330 μm thick sapphire as a substrate due to its low dielectric loss [38]. Each sample is a 8×15 mm chip where the traps and resonators are deposited, as shown in figure 3.1. We design three different trap geometries and three different resonators. Each sample will contain one specific trap geometry and three resonators. Counting with the witness sample (no traps) we have a total of four samples and 12 resonators. Each sample will be coupled to a waveguide as described in section 3.3.

3.1.1 Resonators

The resonators used by *Grunhaupt et al.* are micro-strip $\lambda/2$ resonators made of high resistivity granular Aluminum. It is a rather simple design consisted on a rectangular film, 20 nm, shown in figure 3.1 in green. Resonance frequency is tuned by setting the width w, the length l, and the resistivity of the grAl films. These parameters where chosen such that they resonate all within a GHz range. They were simulated[1] for a kinetic inductance of 2 nH/sq ($R_n = 2\,\mathrm{k}\Omega/\mathrm{sq}$) to have the dimensions and resonant frequencies presented in table 3.1:

TABLE 3.1: Geometric parameters of the resonators and respective simulated resonance frequency, assuming sheet kinetic inductance of $2nH/sq$.

Design Name	w(μm)	l(μm)	f_0(GHz)
A	10	600	6.3
B	40	1000	6.0
C	5	420	6.8

The resonators will couple to the electric field inside waveguide through their dipole moment which depends mostly on their length. Hence, longer resonators will couple better to the waveguide and have lower coupling quality factor. The

---

[1] Simulations done using ANSYS hfss.

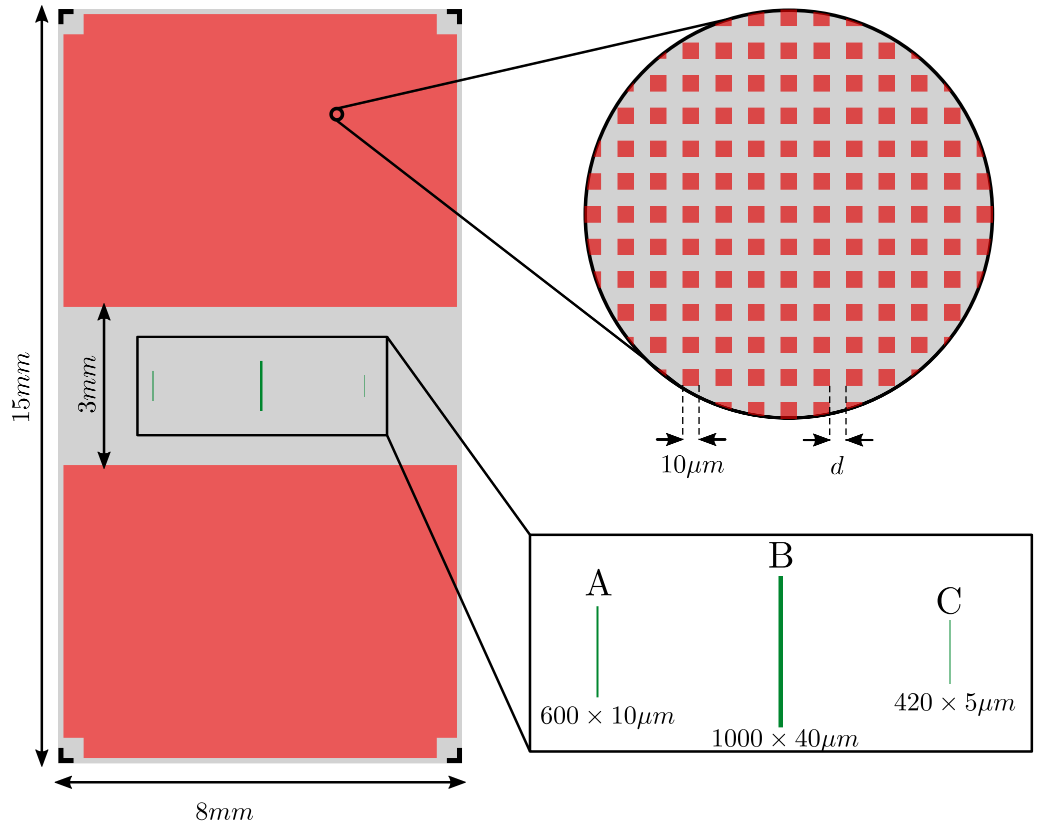

FIGURE 3.1: Schematic of the design of each sample. The sapphire substrate in gray, 15 × 8mm, with 330μm thickness. The phonon traps in red, made of 60nm thick aluminum and consisting on a matrix of small, 10 × 10μm squares with a variable distance d from each other. There is a 3mm in the distribution of traps, where the resonators are placed. Three different resonator geometries in green composed of 20nm thick granular Aluminum.

strength of the electric field also plays a role, resonators in center of the chip will be in the maximum of the electric field of the waveguide and couple stronger. Thus resonator B will be much more coupled than resonators A and C.

3.1.2 Phonon Traps

The traps were design to cover as much area of the chip as possible, while not interfering with the electromagnetic properties of the resonators. From simulations we found that a 3 mm gap in the center of the chip is a safe distance to avoid this. We decided to make traps as 10 × 10 µm squares, arranged in a grid with a distance d between them, as depicted in figure 3.1 in red. We chose a thickness of 60 nm (3 times as thick as the resonators) in order to get better trapping efficiency.

The decision of making the traps in the shape of small squares came from the goal of avoiding Abrikosov vortices, making the area too small for their creation at low magnetic fields, even though the presence of vortexes would effectively lower the gap and possibly improve their efficiency. However we wanted to make the system as simple as possible and the presence of vortexes would add a degree of complexity. Previous works that used a similar strategy to avoid vortexes, used a grid of holes instead of squares[39] (effectively the negative of our design). We didn't follow this strategy due to fabrication limitations. As we are using lithography, fabricating the grid of holes would force us to have thin towers of resist that would not stick well to the substrate. This way we get the same effect without needing to deal with that problem.

We vary the trap filling factor, defined as the ratio of chip surface covered in traps by changing the distance between traps *d*. The parameters for each different trap geometry are shown in table 3.2.

TABLE 3.2: Design parameters of the phonon traps.

Design Name	d(µm)	Filling Factor (%)
0	-	0
1	20	8.5
2	10	19
3	5	34

3.1.3 Wafer

The samples were fabricated in 2 inch sapphire wafers, where it is possible to place 8 samples displayed in two rows of four, as shown in figure 3.2. Due to the way the mask was designed, the 4 top samples contain resonators designed to be used at higher film resistivity, and will not be used in this project.

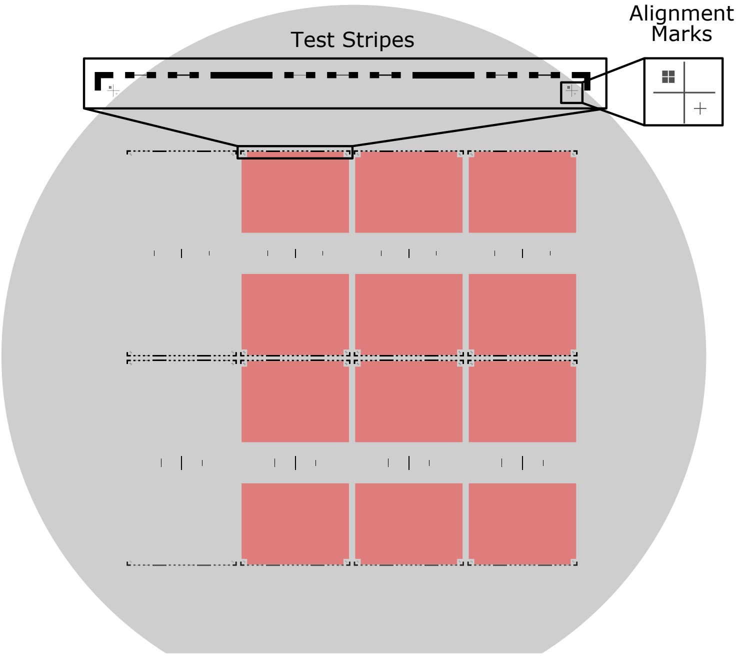

FIGURE 3.2: Schematic of the wafer before dicing. 8 samples per wafer .Top four samples have different resonator geometries that are not used. Density of traps increases from left to right. Each sample has a total of 18 test stripes to measure the resistivity of the film. For a grand total of 144 test stripes. There are also alignment marks to help in the mask alignment, and dicing marks.

Samples are positioned from left to right with trap designs 0, 1, 2 and 3 in that order. Besides the resonators and traps, each sample contains test structures used to measure the resistivity at room temperature. As the circuits are composed of two different materials (Al and grAl) that are evaporated in different steps, alignment marks are added in order to help with the mask alignment.

3.2 Fabrication

In order to fabricate the samples we used reversal optical lithography. We used this instead of the usually used positive optical lithography in order to have an undercut in the resist and avoid the creation of fences that could damage the performance of the resonators as depicted in figure 3.3.

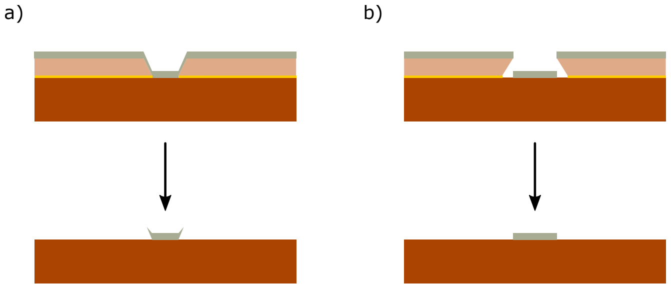

FIGURE 3.3: Cross section of a circuit after evaporation (top) and after lift off (bottom). For (a) positive optical lithography and (b) image reversal optical lithography. In figure (a) there is no undercut and the metal is deposited on the walls of the resist. Creating the fences seen in the bottom. In (b) there exists an undercut and consequently there are no fences after lift off.

Reversal optical lithography is an eight step process which is shown in figure 3.4 and listed below:

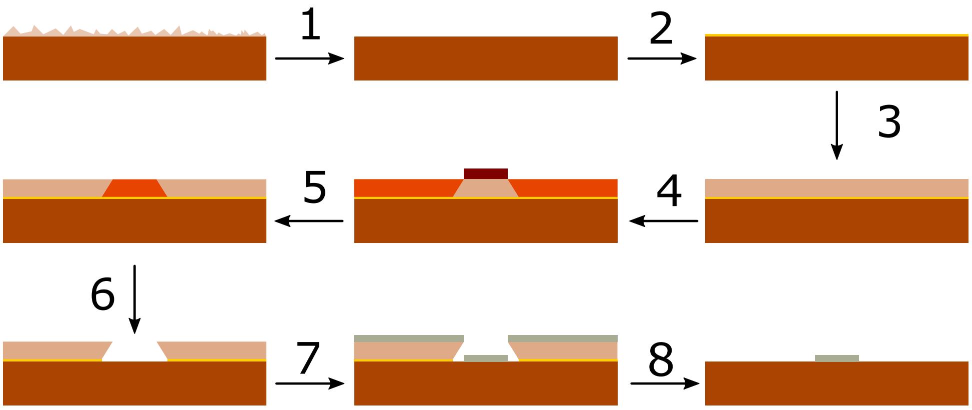

FIGURE 3.4: 8 steps of the fabrication process of image reversal optical lithography. Step by step explanation can be found in the main text.

1. **Piranha clean.** The first step of the fabrication is to clean the wafer of any residual organic matter with the piranha solution (3 parts H_2SO_4 to one part H_2O_2).

2. **Primer application.** A layer of HDMS primer is deposited on the surface of the wafer in order to increase the adherence of the resist to the substrate. The layer

is applied by evaporating a few drops of primer in an excicator (pressurized chamber), which will condensate on the wafer, creating a mono-atomic layer.

3. **Resist application.** A 1.2 µm layer of photoresist is spread on the wafer. In a spincoater a few drops of *AZ 5214E* resist are deposited on the wafer which is then spinned at 6000 rpm for 60 seconds. The wafer is then baked at 110°C for 50 seconds.
4. **Exposure.** A mask containing the design of the circuit is placed on top of the wafer, it is then exposed for 3 seconds to 13 mW/cm^2 of 365 nm UV light. The part of the resist which was not protected by the mask is now active, meaning it is soluble in the developer. The more exposure time the more pronounced the undercut is.
5. **Image reversal.** After the first exposure the active resist has the shape of the negative of the goal circuit. The image is reversed by baking the wafer at 120°C for 60 seconds and by exposing a second time for about 30 seconds, this time the whole sample is exposed. At the end of this step, the previously active resist turns non-active and vice-versa.
6. **Development.** The wafer is submerged in *MIF 726* developer for about 20 seconds, the active resist will be dissolved, leaving only a trench with the geometry of the circuit. The process is stopped by submerging the wafer in water. The exposed primer layer also is dissolved. The development time is one of the most important parameters. If the wafer spends to much time in the developer it could happen that the circuit will have bigger features than expected. In the limit the developer can even crawl under the resist and eliminate the adherence between the resist and the substrate. Not enough development time and the circuit will have smaller features than expected and eliminate the resist undercut.
7. **Evaporation.** Circuit is deposited on the wafer. The wafer is placed in a pressurized chamber, where aluminum is evaporated, and deposits on the wafer. In order to make granular Aluminum a flow of oxygen is added to the chamber. The control of this flow allows the tunning of the sheet resistance of grAl, meaning: more flow, more resistive films. The thickness of the films is controlled by the evaporation rate and time.
8. **Lift-off.** The deposited metal sits now in one of two positions: in contact with the substrate with the shape of the circuit, or on top of the resist. By submerging the wafer in N-Ethil-2-pyrrolidone (NEP) heated at 90°C for 1h30 the remaining resist is dissolved and the metal sitting on top of it without any support is no longer attached to the wafer, leaving only the final circuit. Finally any residual resist is removed by submitting it to sonication, and being rinsed in acetone, ethanol and water.

This steps are preformed a first time for the resonators, and repeated a second time with exception of step 1 for the traps. The only difference being the presence of oxygen in the evaporation step for the grAl films (resonators).

The wafer is then diced and the different chips are ready for mounting.

3.3 Sample Mounting

After dicing, the samples are glued to a waveguide, as depicted in figure 3.5a. The waveguide used in this work is a hollow copper box, that serves as a transmission line to which the resonators couple capacitively. A copper coaxial cable is coupled to the waveguide through an orifice in the top, it also contains two screws that are used to fine tune the impedance matching to the coax cable, by changing the geometry of the waveguide interior. The samples are glued to the waveguide with silver paste for better thermalization. Two waveguides containing a sample each are screwed to a copper rod as depicted in figure 3.5b.

The copper rod is then inserted into a barrel 3.5c. The barrel is made of 3 layers of different materials which serve as shielding against exterior radiation and magnetic fields. The first layer is made of copper, which is easily thermalized, in order to have low levels of black body radiation in the proximity of the samples. The second layer is made of aluminum which at operation temperature turns superconducting and due to the Meissner effect shields against exterior magnetic fields. The most exterior layer is made out of μ-metal which further increases magnetic shielding. In this way, each barrel will be shared by two samples, which means we will have two barrels in the cryostat.

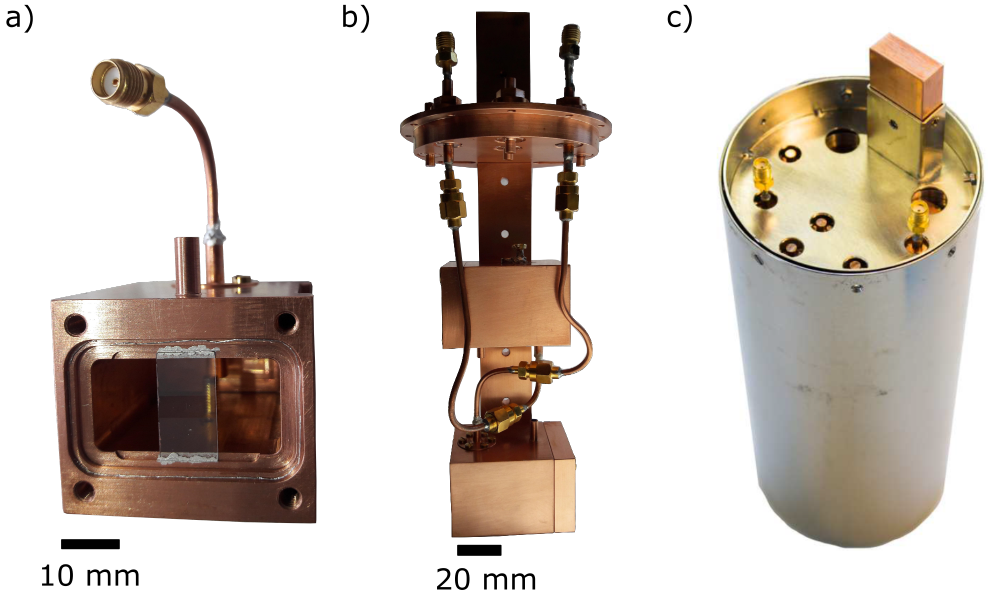

FIGURE 3.5: (a) Example of a sample mounted into a waveguide, the sample is glued to it with silver paste. The connector is coupled to the waveguide with a copper cylinder that extends to the interior. The four holes seen in the front of the waveguide will be used to screw in its lid. (b) Example of two waveguides screwed to the copper rod; coper is used due to its high thermal conductivity, waveguides are connected to the exterior by copper coaxial cables connected to the top plate of the rod. (c) Exterior μ-metal shields. Remaining shields sit in the inside.

3.4 Measurement Setup

The measurements were taken in a dilution cryostat, which allow us to reach a base temperature of approximately 15 mK. The fridge is composed of several temperature stages, namely 60 K, 4 K, the still at 500 mK, a heat exchanger stage at ("cold stage") 100 mK and the base stage at 15 mK. The fridge has 3 shields each attached to a different stage. The first shielding is attached to the room temperature stage, the second to the 4 K stage and the third to the Still stage. The shields are separated by vacuum. 15 mK temperature is achieved by ^{4}He and ^{3}He mixing as described in [40].

A schematic of the electronics inside the cryostat are shown in figure 3.6.

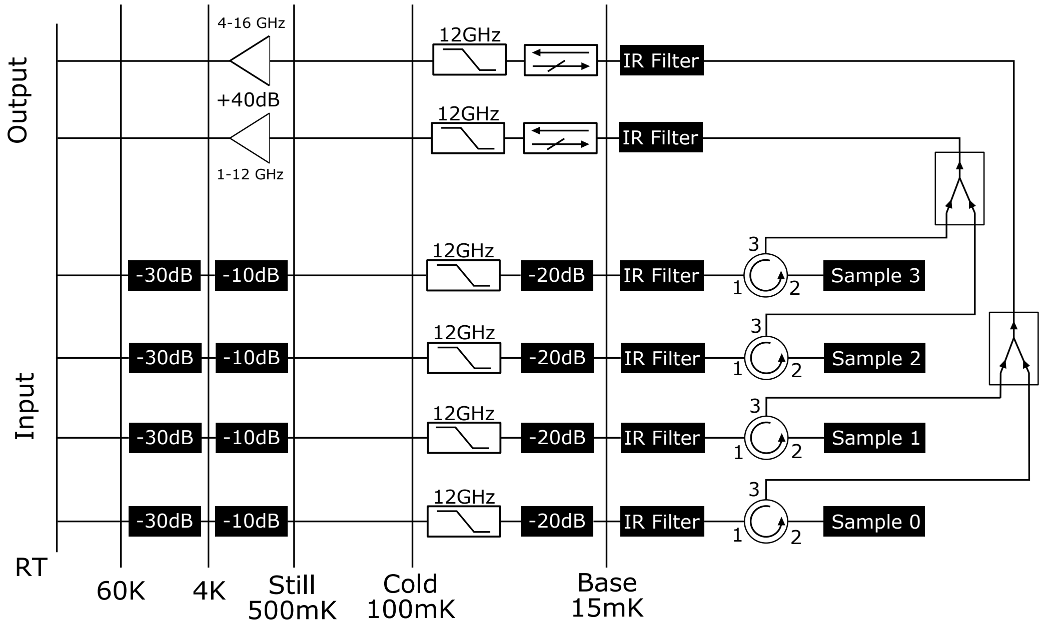

FIGURE 3.6: Electric wiring of the fridge. The input lines are identical for all 4 samples. Having a 30 dB attenuator in the 60 K stage a 10 dB attenuator in the 4 K stage, a low pass filter with 12 GHz of cutoff frequency and a 20 dB attenuator at the 100 mk stage, and an infrared filter at base. The input and reflected signals are separated with a circulator. Samples are connected in pairs that share the same output, signal mixing is done with a combiner. The output line contains an infra-red filter at base, a signal gate and a 12 GHz low pass filter in the 100 mk stage and finally 40 dB amplifiers of 4 to 16 GHz or 1 to 12 GHz depending on the line.

In order to attenuate room temperature noise and to successfully thermalize the input lines, it is required to have an array of attenuators distributed over multiple temperature stages of the cryostat. This way, typical reflection measurements only using one line are impossible, because the reflected signal would be attenuated on its way up the line. The strategy to solve this is to connect a circulator in the input of the sample and perform transmission measurements instead. A circulator is a 3 port device that only allows signal to pass through neighboring ports in a specific order (from ports 1 to 2, 2 to 3 and 3 to 1). This way the input signal will be sent through port 1 and go to the sample (port 2), while the reflected signal goes from port 2 into the output line (port 3). Measurements of the transmission at the ports of the circulator will be the same as reflection measurements at the output of the waveguide.

Furthermore there are only two output lines available, hence samples share output lines in pairs. The output signal from each pair of samples is routed using a combiner.

Besides attenuation, which sums to a total of 60 dB in the fridge, the input lines also have a 12 GHz low pass filter in the 100 mK stage and an infra-red filter at base. The IR filter is also present in the output line along with an isolator to avoid signal from the exterior to reach the samples through the output lines, a 12 GHz low pass filter and a 40 dB amplifier, with an active range of 4-16 GHz or 1-12 GHz depending on the line.

The signal is then analyzed at room temperature by a vector network analyzer. At room temperature, a 20 dB attenuator is added to the input line in order to reach the single photon regime, and a 40 dB amplifier to the output to further amplify the signal, for a total of 80 dB attenuation in the input line and 80 dB amplification in the output. Note that these values of attenuation are an estimate because the cables also add some attenuation.

Chapter 4

Results

4.1 Finding the Resonators

On the 14 GHz frequency range of the vector network analyzer we have to find our resonators, each with a bandwidth in the order of 5 to 40 MHz. Once found, we fit the reflection parameters with the method described in [23], which gives us the resonance frequency f_0 and the coupling and internal quality factors Q_c and Q_i. As the resonators sit in a background of cable resonances and residual impedance mismatches, the data has to be corrected before fitting, following the method described in appendix A. An example of corrected and fitted data can be found in figure 4.1, for resonator 2C at an input power of $-85dBm$ at the entrance of the waveguide.

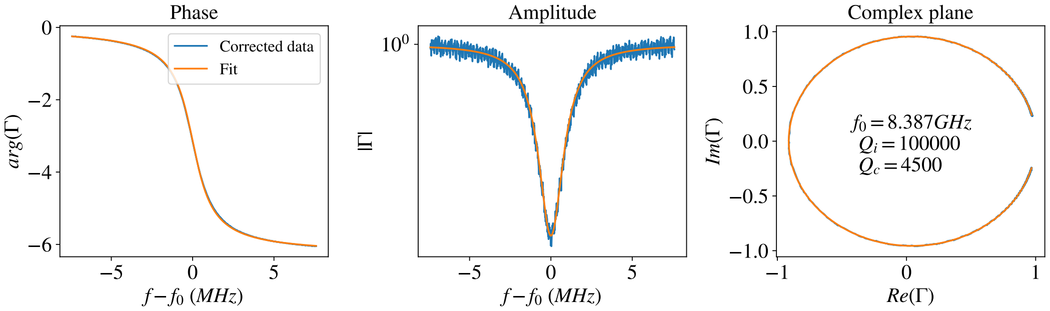

FIGURE 4.1: Example of a fitted resonator. Resonator 2C at a power of -85dBm at waveguide corresponding to a average photon number $\bar{n}$ =1.8 × 10^5.

Out of the twelve resonators we were able to find eleven. Resonator 3B[1] was not found as it probably was sitting in a frequency range where the impedance mismatchings turned it unrecognizable. The resonance frequencies and coupling quality factors of the remaining can be found in figure 4.2[2].

We notice in figure 4.2, that the resonators have higher frequency then expected. The average measured sheet resistance of the film at room temperatures is 2.5 kΩ/sq, using equation 2.28 we would expect a sheet kinetic inductance of 2.3 nH/sq, simulating resonators A give us a resonance frequency of approximately 5 GHz. The discrepancy between simulated and measured values is most probably due to the deviation of equation 2.28 from reality for grAl. For highly resistive films, grAl is

---

[1] For more information about the nomenclature of the resonators check section 3.1.1

[2] The color schemes used in this figure will be used throughout the text. The scheme in (a) for grouping by samples. The scheme in (b) for grouping by resonator geometry

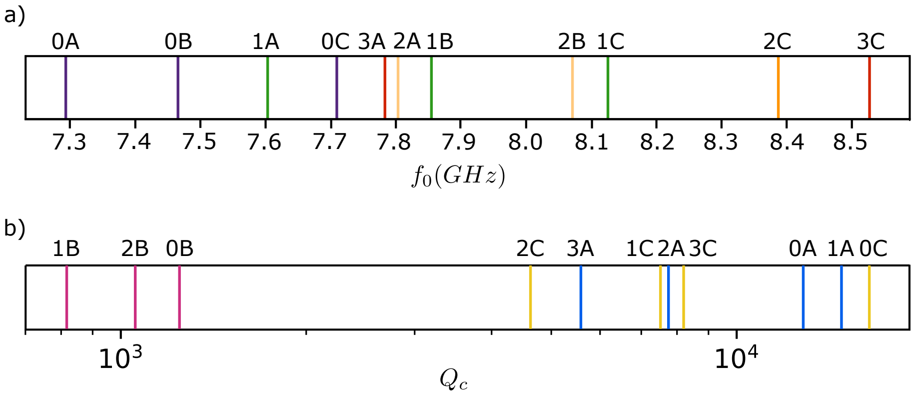

FIGURE 4.2: (a) Plot of the resonance frequencies of the resonators. Samples 0, 1, 2, 3 in purple, green, orange and red respectively. (b) Coupling quality factors. Resonator geometries A, B and C in blue, pink and yellow.

no longer a conventional superconductor and the formula breaks down. Furthermore, equation 2.28 refers to a resistance at a temperature before the superconducting phase transition, not at room temperature. For most materials the deviation from these two values is negligible, but for high resistivity grAl it can be unpredictable.

The resonance frequency seems to increase with the density of traps, which is thought to be an artifact. We measured a gradient of sheet resistance of 3.1 to 2.2 kΩ/sq in the wafer after fabrication as shown in figure 4.3, which results in a difference of kinetic inductance from sample to sample that reasonably explains the deviation. This gradient is due to spacial fluctuations of the partial pressure of oxygen in the chamber during evaporation, and could have been avoided by rotating the sample during evaporation.

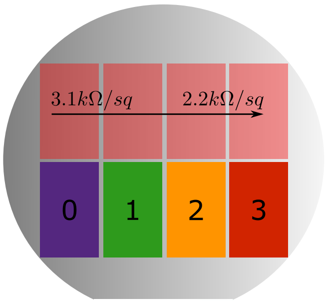

FIGURE 4.3: Schematic of the resistance gradient in the wafer. From sample 0 to sample 3 there is a gradient from 3.1 to 2.2 kΩ/sq.

Lastly, we see from figure 4.2b that resonators B have much lower coupling quality factor then the others, which is expected for the largest resonators. From simulation (table 3.1) it would be expected for these resonators to have the lowest resonance frequency. This leads us to assume that resonators A and B traded positions in the spectrum. This can be explained by a $\approx 1\,\mu\mathrm{m}$ decrease of width from the width used in the simulation, which is a reasonable assumption given the precision of the optical lithography.

4.2 Dissipation Performance

We monitor the internal quality factor of each resonator as a function of average photon number populating the resonator (using equation 2.22) in order to test the efficiency of phonon traps in minimizing the density of quasi-particles and dissipation. The results are shown in figure 4.4.

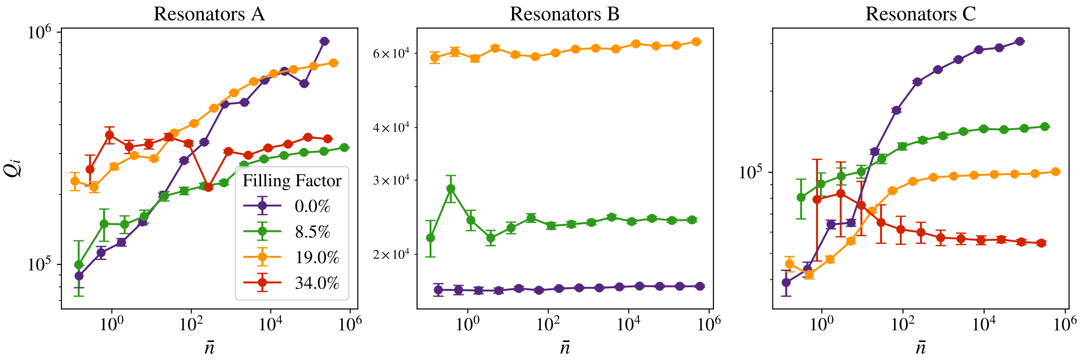

FIGURE 4.4: Internal quality factor for all resonators in function of average photon number.

At $ff = 0\%$ the behavior of Q_i in function of $\bar{n}$ is in agreement with the model presented in section 2.2.3 and [37]. Where it is considered that in $grAl$ there are two distinct species of quasi-particles, mobile and localized. The latter are trapped in a potential well and cannot move and recombine. The mobile QP on the other hand can flow through the film and recombine more easily. Hence the more mobile QP the more recombination and the less density of quasi-particles there is. It can be demonstrated that the higher the density of current the more localized QP can be excited to the mobile state. Meaning that the higher the photon number the less QP and higher Q_i. In the resonators B this effect is not visible because the resonator is much wider and the density of current is lower, and not high enough to excite localized quasi-particles, thus Q_i does not depend on $\bar{n}$.

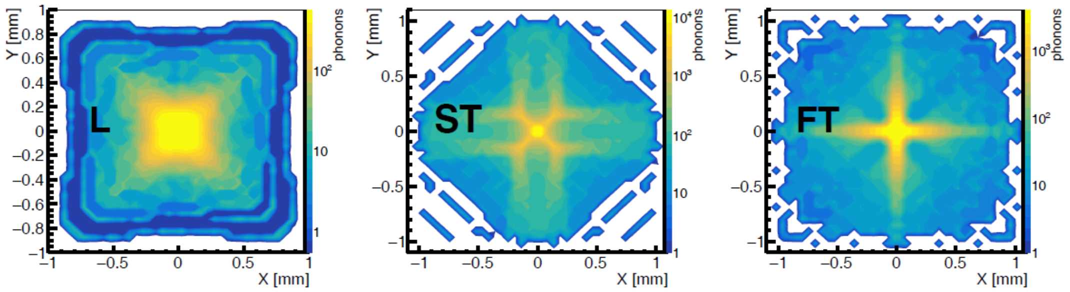

FIGURE 4.5: Results of a Monte-Carlo simulation of the phonon propagation in 2×2 mm silicon substrates.The panels show the phonon intensity in the surface of the substrate for every polarization: longitudinal (left), slow transversal (center) and fast transversal (right). Phonons were simulated to be generated in the center of one of the substrates face and detected in the opposite. Phonon focusing structures (bright colors) are clearly formed in the center of the chip, especially for the transverse modes. Figure taken from *Martinez et al.* [41].

One might regard that resonators B have lower Q_i, in the order of a 10^4 while the remaining resonators have Q_i in the order of 10^5. As shown by *Martinez et al.* [41]

and figure 4.5, phonon propagation in the substrate tends to concentrate in the center of the chip where resonator B is positioned. Hence, resonators B shall have more creation of QP due to phonons and have lower quality factor. Which indicates that the position of the circuit in the chip as an influence on the quasi-particle density. It is important to specify that the results from *Martinez, et al.* where taken from a Monte-Carlo simulation for a silicon substrate with different geometry the the ones used in this project. In order to have a quantitative interpretation of this result, simulations have to be made for sapphire and for the chip geometry of this work.

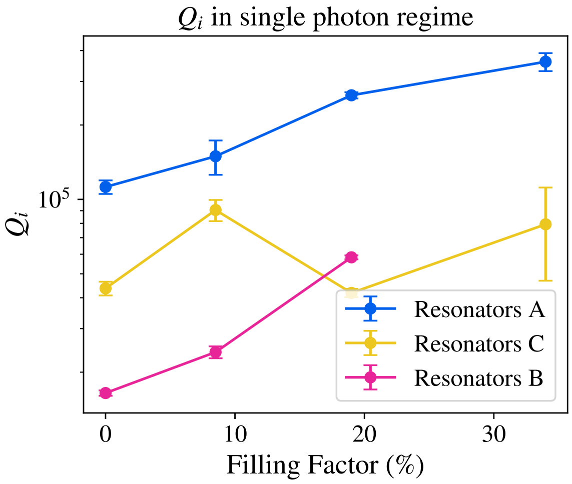

FIGURE 4.6: Internal quality factor for all resonator geometry in function of filling factor in the single photon regime.

At single photon it is observed that, with exception for resonators C, the quality factor reliably increases with filling factor, as plotted in figure 4.6, an indicator of the efficiency of phonon trapping in this regime. Which is the functioning regime of superconducting qubits.

On the other hand, at high photon number, this tendency appears to be inverted in resonators C and disappears in resonators A. The explanation for this inversion is unknown, but it is reasonable to assume that phonons have a role on the dynamics of mobile and localized QP in $grAl$.

4.3 Noise Performance

If there is a random rate of creation/annihilation of QP in the resonator, the resonance frequency will follow accordingly as stated in equation 2.31. As it is impossible to resolve the full reflection parameters quickly enough to see significant frequency shifts, we study time evolution of the resonance frequency by implementing a technique called time-traces. In a time-trace we choose a measurement frequency f_m, close to the resonance frequency and evaluate the phase response over time. As we have the full phase response from previous measurements we are able to fit it and inverse it to extract the resonance frequency as a function of time. If the phase roll off takes the form:

$$\phi(f) = \phi_0 + m \ \arctan\left(a(f - f_0)\right) \tag{4.1}$$

Then the resonance frequency over time is given by:

$$f_0(t) = f_m - \frac{1}{a} \tan\left(\frac{\phi(t, f_m) - \phi_0}{m}\right) \tag{4.2}$$

For f_m close to the resonance frequency, and for small phase fluctuations, a shift in resonance frequency is proportional to a shift in phase $\delta f_0 \propto \delta\phi_0$, and doing noise analysis with the phase signal is equivalent to doing it with the resonance frequency.

In order to study the noise of a time-trace we calculate its noise spectral density (NSD) defined as:

$$nsd(f) = \frac{\sqrt{|\mathscr{F}\{\phi(t)\}|^2}}{\sqrt{BW}} \tag{4.3}$$

where BW is the bandwidth defined as the inverse of twice the total time of the trace, and $\mathscr{F}$ is the Fourier transformation.

When analyzing the noise of the resonators we come across to two phenomena depicted in figure 4.7.

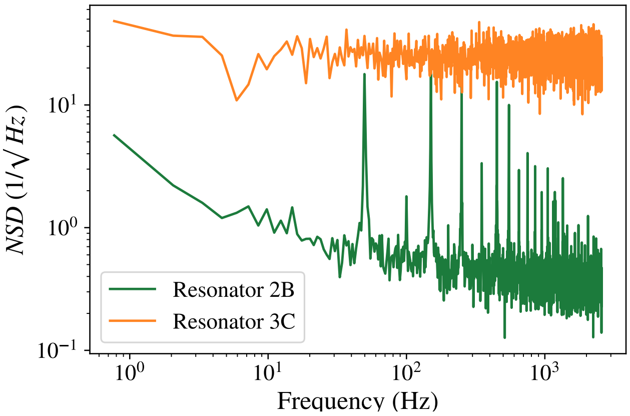

FIGURE 4.7: Noise spectral density for resonators 3C and 2B the latter acts as an example for all resonators B. −95 and 75 dBm power at the waveguide for resonators B and C respectively.

The first is that resonator 3C, that has the highest resonance frequency, is subject to a higher noise level then the remaining resonators. This is due to the fact that it sits outside the operational frequency range of the circulator that has a range of 4-8 GHz. The second phenomenon is that in all resonators B, we see strange peaks in the noise spectrum. As they are the resonators with larger features, the maximum number of photons that can populate the resonator before bifurcation is much higher, and as such we can drive them at higher powers, consequently the NSD is low enough to reveal this peaks. The first of these peaks sits at approximately 50 Hz, while the remaining seem to be harmonics of the first. This lead us to assume that this noise comes from the public electric grid.

In the resonators with no traps (sample 0), when evaluating the time tracers, we observed low frequency high amplitude fluctuation of the compatible with $1/f$ noise. To prove that these fluctuations come from the resonator and not from the circuit, we took time traces away from any resonator at 7.37 GHz (between resonators 0A and 0B), and there are no fluctuations, making us assume that these fluctuations come from the resonators, most probably due to cooper pair breaking from external sources, possibly mediated by phonons.

If a source of noise comes directly from the resonator, and not from the electric lines, then it should not depend on the input power. That said, in figure 4.8 we show the NSD for resonator 0A at different input powers.

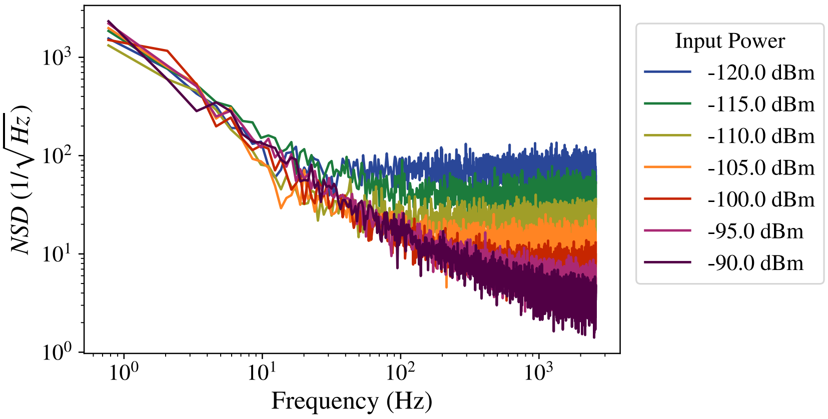

FIGURE 4.8: Noise spectral density for resonator 0A for several different input powers.

We see two distinct features: at high frequencies there is a floor whose level depends on the power, eventually disappearing at $\approx -90\,\mathrm{dBm}$. At low frequencies we observe a slope that is independent of power. This is the $1/f$ noise that can be phenomenologically modeled as:

$$nsd(f) = \frac{A}{f^{\alpha}} \tag{4.4}$$

To test this hypothesis, we measured 100 time traces for each resonator at the highest power before bifurcation. Each time trace has about 3.8 seconds and 20 001 points, giving us a resolution of about 200 µs. With the time-traces we calculated the nsd, smoothed it, and fitted equation 4.4 as exemplified in figure 4.9. The $1/f$ fit is performed only on the portion of the noise which does not depend on power, for simplicity we used the nsd at frequencies lower than 30 Hz. Time traces containing stochastic bursts (see section 4.4) where not used.

The results shown in figure 4.10 are the averages of α and A obtained from the fits.

We see that the amplitude of the noise decreases with the filling factor for all resonator geometries, even by a factor 10 in resonators B, being a good indicator for the good performance of the traps.

α on the other hand also decreases but not as consistently. Resonators A and B show a clear decrease reaching a point of saturation where it seems adding more traps does not affect α. In resonators C however we see a first decrise from $ff = 0$ to $ff = 8.5\%$ but it goes back to the original value at $ff = 19\%$. Comparing the results with the internal quality factors at single photon of figure 4.6 we see the same tendency, traps with $ff = 19\%$ specifically for this resonator seem to have as much effect as no traps.

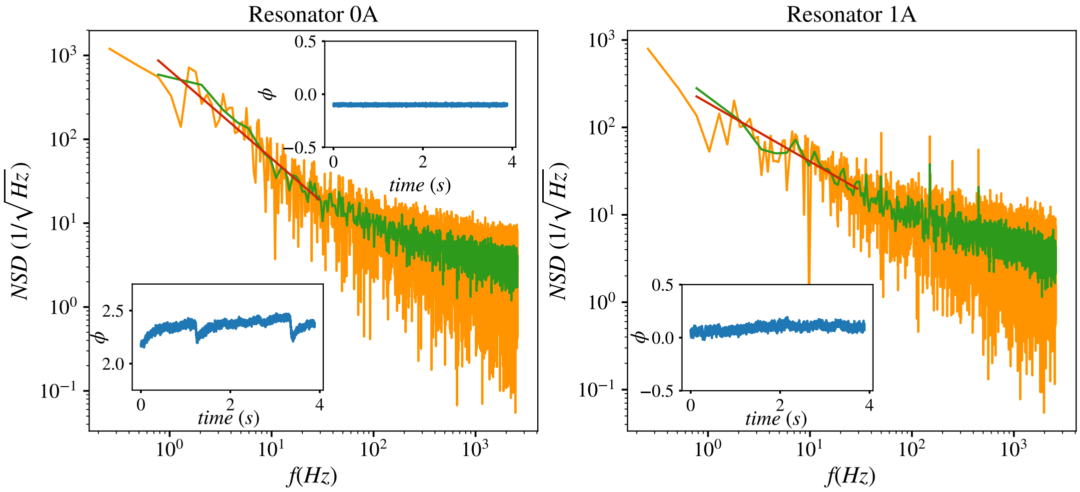

FIGURE 4.9: Raw noise spectral density in yellow. Smothed nsd in green and $1/f$ fit in red. Time traces in blue: for resonator 0A in the bottom left corner of the left window, away from any resonator in sample 0 in the top right corner, and 1A in the left bottom corner of the right window. Time traces are all shown with the same phase span in order to be possible to compare the noise levels.

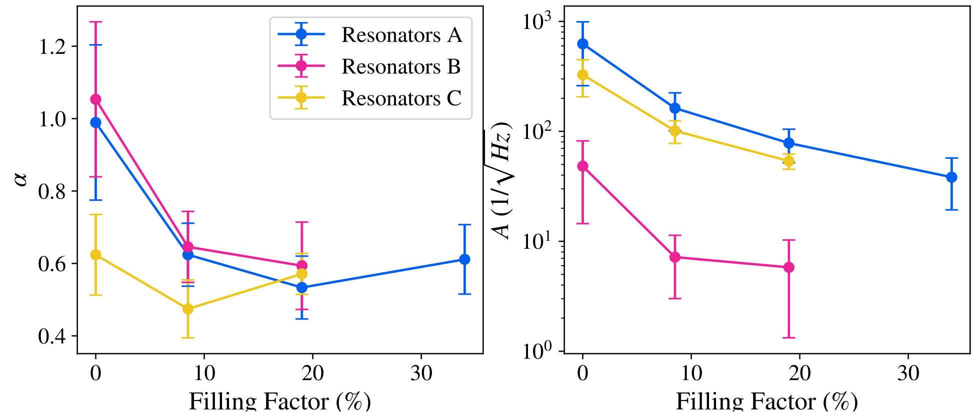

FIGURE 4.10: Results of the $1/f$ noise fitting for all resonators except 3C. Left α, right A.

Compairing these results with the internal quality factor at high photon number, for which the nsd measurements were done, we see that the tendency is inverted: loss increases with filling factor while noise decreases. Which makes us consider the possibility that at high powers loss is dominated by an other sources besides quasi-particles.

4.4 Stochastic Bursts

It is observed that approximately every 20 seconds the resonance frequency drops abruptly as exemplified in figure 4.11, in agreement with a rapid creation of a high number of QP.

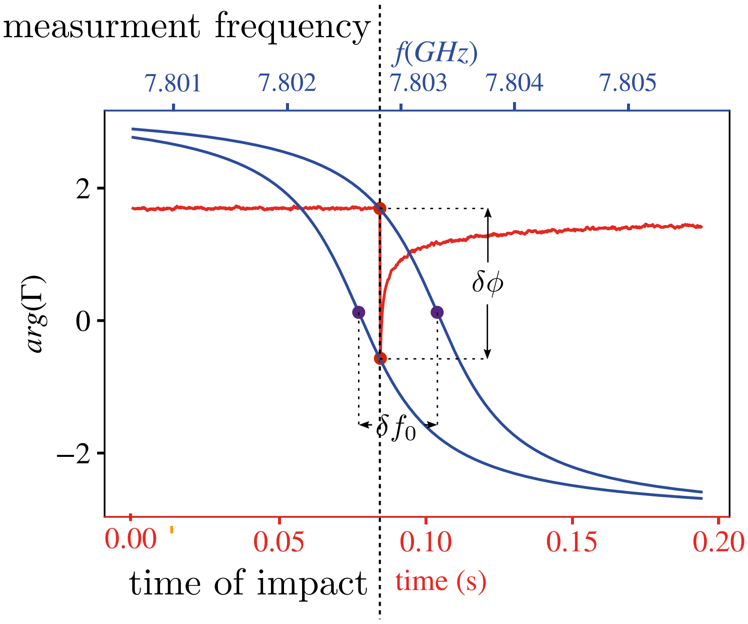

FIGURE 4.11: Full trace and time trace of an event. In yellow a time trace of an event. In green the full phase response just before and after the event. It is shown the correspondence between a phase shift in the time trace $\delta\phi$ with the resonant frequency shift δf_0.

This phenomena was first observed in granular Aluminum by *Grunhaupt et al.*[37]. In his work it was observed that the bursts are characterized by an initial fast drop of f_0, too fast to be resolved by our electronics, followed by a rapid $1/t$ decay and lastly an exponential tail with characteristic times in the order of a second. It was also seen that the time between successive events follows a Poisson distribution with a characteristic time of 19 seconds, which implies that the time of the bursts are independent of each other and random. Furthermore, long time traces taken over several days don't show any significant difference between day and night, which is an indicator that the source of the events do not originate on the sun. The source is still unknown but it is though that it could be cosmic muons, as they reach earth with a rate consistent with the measurements (within an order of magnitude), or parasitic radioactivity on the materials surrounding the samples.

If we assume that the particles that create these events hit the substrate (not directly the resonators) creating phonons that act as mediators for the impact, then adding phonon traps should lower the number of phonons reaching the circuit thus reducing the intensity of the bursts and effectively lowering the rate of detectable events. We measured long time traces, of about a day for each resonator, and detected the events. In fact, as shown in figure 4.12 the rate of detectable events decreases with the trap filling factor. Suggesting that the bursts are mediated by phonons and the usage of phonon traps reduces significantly the number of phonons responsible for the bursts.

We further test this hypothesis by measuring the frequency shift for all detected bursts. The results are shown in the histograms of figure 4.13.

In resonators B the tendency is clear, the rate of events detected decreases with the filling factor, as does the maximum normalized frequency shift, indicating that the traps work reliably in suppressing events for this resonators in particular. We

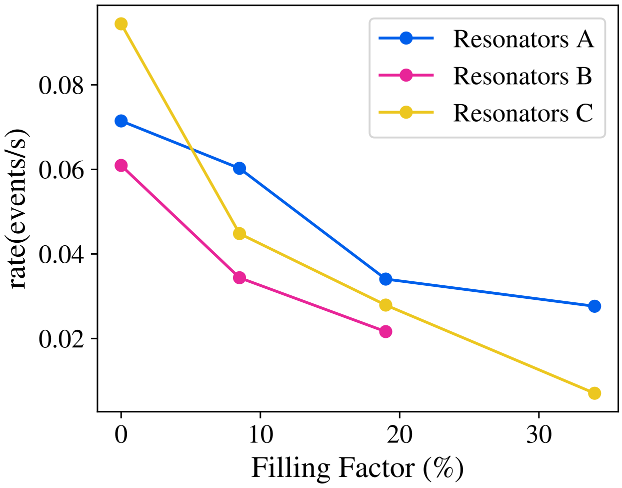

FIGURE 4.12

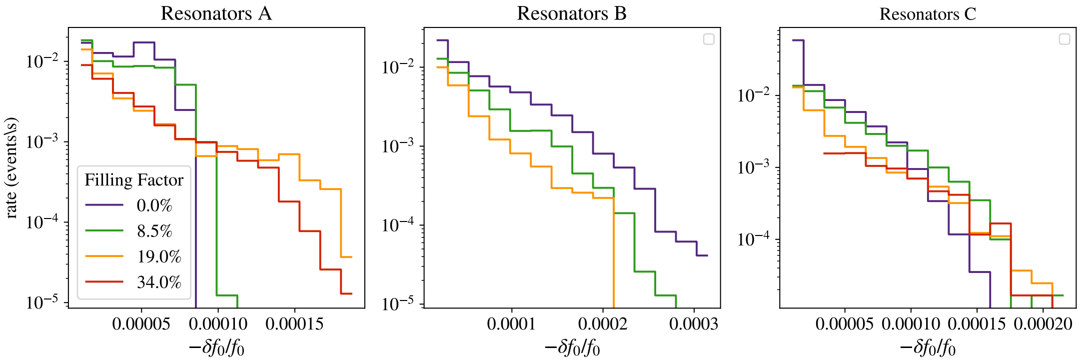

FIGURE 4.13: Histograms of the resonance frequency shift of the events. The frequency shift is normalize to the resonance frequency before the impact, while the event rate is defined as the number of measured events over the total measurement time.

suggest that the frequency shifts in these resonators is slightly higher due to the concentration of phonons in the center of the chip, however this argument is not strong due to the high differences between resonator geometries, which results in different kinetic inductance (which quantifies the sensibility to QP) and in the total number of charge carriers.

Resonators A and C on the other hand, don't show the same obvious behavior. There is a tendency at low frequency shifts for the event rate to decrease with the filling factor. However the maximum frequency shift does not decrease with the filling factor, which is evident in resonators A and there is still no clear explanation for this phenomena.

Chapter 5

Conclusion

We measured 11 resonators in 4 chips, each with different trap filling factor, and observed that for resonators B ($1000\times40\,\mu$m) the results support our starting hypothesis. By using phonon traps we successfully increased the internal quality factor, suppressed the $1/f$ noise and decreased the rate of stochastic bursts and their maximum energy, proving phonon propagation as an important source of quasi-particles generation in superconducting circuits, and phonon trapping as a reliable solution. For the resonators A and C ($600\times10\,\mu$m and $420\times5\,\mu$m respectively) the results are not as clear, seen that the internal quality factor was only improved in the single photon regime with the exception of resonator 2C ($ff = 19\%$). The behavior of internal quality factor at high photon number for this resonators is at the moment unexplained. The $1/f$ noise was reliably suppressed, with exception once again of resonator 2C, making us assume that there is some unexplained phenomena with this resonator in particular. For most resonator geometries the strength of the stochastic bursts was decreased, effectively decreasing the rate of detectable events.

Effectiveness of the phonon traps can be further improved by increasing the filling factor, the thickness of the traps and the superconducting gap difference between traps and circuit. Performing phonon propagation simulations similar to those described in *Martinez et al.* [41] can be useful in order to find the right trap placement, which for this case it would be the center of the chip. These improvements should be tested in future projects. Furthermore, the model formulated by *Valenti et al.* [35] and presented in section 2.4, can possibly be used to explain the results quantitatively.

Concluding, superconducting circuits are susceptible to phonon propagation, and circuits where loss or noise is dominated by quasi-particles can be improved by the addition of phonon traps. We believe that for most circuits, phonon traps of the type used in this work should be easy to implement and effective.

Appendix A

Resonator Fitting Algorithm

In order to fit the reflection coefficient of each resonator it is used the method described in [23]. For resonators sitting in a landscape of arbitrary resonances and impedance mismatches it is required to first correct the data. 2 transformations are aloud to be performed without interfering with the physical meaning of the fits: rotation of the circle around the center of the complex plane and rotations around the center of the circle. In order to have the typical dip in the amplitude response, the detuned and at resonance reflection coefficients, Γ_d and Γ_0 have to be collinear with the center of the complex plane and the center of the circle. Thus, for resonator where this is not the case, the correction is made by rotation the circle to its center by an angle α as depicted in figure A.1.

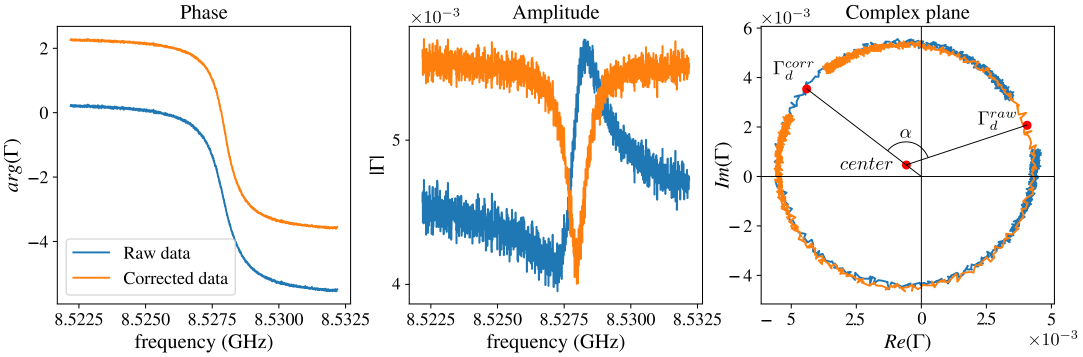

FIGURE A.1: Example of the reflection coefficient correction for resonator 3C at an input power of -90dBm. In blue the original data and in orange the correction. In the complex plane representation, the detuned refflection coefficients are represented as Γ_d^{raw} for the raw data and Γ_d^{corr} for the corrected data. The center of the circle and the rotational angle α are also represented. The results of the fit where $Q_l = 7241$, $Q_i = 55952$, $Q_c = 8318$ and $f0 = 8.528$ GHz

The circle is once again rotated but this time around the center of the plane so that the detuned and in resonance reflection both sit in the real axis. This transformation is nothing more than a simple addition or subtraction of a phase offset. Lastly the amplification/attenuation are corrected by rescaling the radius of the circle to be one. After these transformations the reflection coefficient is ready for fitting.

Bibliography

[1] Peter K. Day et al. "A broadband superconducting detector suitable for use in large arrays". In: *October* 425.October (2003), pp. 12–14. DOI: `10.1038/nature01981.1.`.

[2] D. Drung et al. "Low-noise high-speed dc superconducting quantum interference device magnetometer with simplified feedback electronics". In: *Applied Physics Letters* 57.4 (1990), pp. 406–408. ISSN: 00036951. DOI: `10.1063/1.103650`.

[3] O. Naaman and J. Aumentado. "Time-domain measurements of quasiparticle tunneling rates in a single-Cooper-pair transistor". In: *Physical Review B - Condensed Matter and Materials Physics* 73.17 (2006), pp. 4–7. ISSN: 10980121. DOI: `10.1103/PhysRevB.73.172504`. arXiv: `0602004 [cond-mat]`.

[4] Hanhee Paik et al. "Observation of high coherence in Josephson junction qubits measured in a three-dimensional circuit QED architecture". In: *Physical Review Letters* 107.24 (2011), pp. 1–5. ISSN: 00319007. DOI: `10.1103/PhysRevLett.107.240501`. arXiv: `1105.4652`.

[5] J. Majer et al. "Coupling superconducting qubits via a cavity bus". In: *Nature* 449.7161 (2007), pp. 443–447. ISSN: 14764687. DOI: `10.1038/nature06184`. arXiv: `0709.2135`.

[6] Austin G. Fowler et al. "Long-range coupling and scalable architecture for superconducting flux qubits". In: *Physical Review B - Condensed Matter and Materials Physics* 76.17 (2007), pp. 1–7. ISSN: 10980121. DOI: `10.1103/PhysRevB.76.174507`. arXiv: `0702620 [cond-mat]`.

[7] P. Bunyk, E. Hoskinson, and M. W. Johnson. "Architectural considerations in the design of a superconductingquantum annealing processor". In: *IEEE Transactions on Applied Superconductivity* 24.4 (2014), p. 1700110.

[8] N. K. Langford et al. "Experimentally simulating the dynamics of quantum light and matter at deep-strong coupling". In: *Nature Communications* 8.1 (2017), pp. 1–9. ISSN: 20411723. DOI: `10.1038/s41467-017-01061-x`. arXiv: `1610.10065`. URL: `http://dx.doi.org/10.1038/s41467-017-01061-x`.

[9] John M. Martinis et al. "Decoherence in Josephson qubits from dielectric Loss". In: *Physical Review Letters* 95.21 (2005), pp. 1–4. ISSN: 00319007. DOI: `10.1103/PhysRevLett.95.210503`. arXiv: `0507622 [cond-mat]`.

[10] V. Zaretskey et al. "Spectroscopy of a Cooper-pair box coupled to a two-level system via charge and critical current". In: *Physical Review B - Condensed Matter and Materials Physics* 87.17 (2013), pp. 1–9. ISSN: 10980121. DOI: `10.1103/PhysRevB.87.174522`. arXiv: `1305.3962`.

[11] S. E. De Graaf et al. "Direct Identification of Dilute Surface Spins on Al2 O3: Origin of Flux Noise in Quantum Circuits". In: *Physical Review Letters* 118.5 (2017), pp. 1–5. ISSN: 10797114. DOI: `10.1103/PhysRevLett.118.057703`. arXiv: `1609.04562`.

[12] Chen Wang et al. "Measurement and Control of Quasiparticle Dynamics in a Superconducting Qubit". In: (2014). ISSN: 2041-1723. DOI: `10.1038/ncomms6836`. arXiv: `1406.7300`. URL: `http://arxiv.org/abs/1406.7300{\%}0Ahttp://dx.doi.org/10.1038/ncomms6836`.

[13] Ioan M. Pop et al. "Coherent suppression of electromagnetic dissipation due to superconducting quasiparticles". In: *Nature* 508.7496 (2014), pp. 369–372. ISSN: 14764687. DOI: `10.1038/nature13017`. URL: `http://dx.doi.org/10.1038/nature13017`.

[14] K. Serniak et al. "Hot non-equilibrium quasiparticles in transmon qubits". In: (2018). arXiv: `1803.00476`. URL: `http://arxiv.org/abs/1803.00476`.

[15] P. J. De Visser et al. "The non-equilibrium response of a superconductor to pair-breaking radiation measured over a broad frequency band". In: *Applied Physics Letters* 106.25 (2015). ISSN: 00036951. DOI: `10.1063/1.4923097`. arXiv: `1505.06191`.

[16] John M. Martinis, M. Ansmann, and J. Aumentado. "Energy decay in superconducting josephson-junction qubits from nonequilibrium quasiparticle excitations". In: *Physical Review Letters* 103.9 (2009), pp. 1–4. ISSN: 00319007. DOI: `10.1103/PhysRevLett.103.097002`. arXiv: `0904.2171`.

[17] Antonio D. Córcoles et al. "Protecting superconducting qubits from radiation". In: *Applied Physics Letters* 99.18 (2011). ISSN: 00036951. DOI: `10.1063/1.3658630`. arXiv: `1108.1383`.

[18] R. P. Riwar et al. "Normal-metal quasiparticle traps for superconducting qubits". In: *Physical Review B* 94.10 (2016), pp. 1–10. ISSN: 24699969. DOI: `10.1103/PhysRevB.94.104516`. arXiv: `1606.04591`.

[19] L. Cardani et al. "Energy resolution and efficiency of phonon-mediated kinetic inductance detectors for light detection". In: *Applied Physics Letters* 107.9 (2015), pp. 1–6. ISSN: 00036951. DOI: `10.1063/1.4929977`. arXiv: `1505.04666`.

[20] L. Cardani et al. "High sensitivity phonon-mediated kinetic inductance detector with combined amplitude and phase read-out". In: *Applied Physics Letters* 110.3 (2017), pp. 1–6. ISSN: 00036951. DOI: `10.1063/1.4974082`. arXiv: `1606.04565`.

[21] David M. Pozar. *Microwave Engineering*. 1998.

[22] Michael Tinkham. *Introduction to Superconductivity*. 1973.

[23] S. Shahid et al. "Reflection type Q-factor measurement using standard least squares methods". In: *IET Microwaves, Antennas & Propagation* 5.4 (2011), p. 426. ISSN: 17518725. DOI: `10.1049/iet-map.2010.0395`. URL: `http://digital-library.theiet.org/content/journals/10.1049/iet-map.2010.0395`.

[24] Philip Krantz. "The Josephson parametric oscillator - From microscopic studies to singleshot qubit readout". PhD thesis. Chalmer, 2013.

[25] J. Bardeen, L. N. Cooper, and J. R. Schrieffer. "Theory of superconductivity". In: *Physical Review* 108.5 (1957), pp. 1175–1204. ISSN: 0031899X. DOI: `10.1103/PhysRev.108.1175`. arXiv: `1101.0277`.

[26] G. Deutscher et al. "Transition to zero dimensionality in granular aluminum superconducting films". In: *Journal of Low Temperature Physics* 10.1-2 (1973), pp. 231–243. ISSN: 00222291. DOI: `10.1007/BF00655256`.

[27] Roger W. Cohen and B. Abeles. "Superconductivity in Granular Aluminum Films". In: *Physical Review* 109.1954 (1967).

[28] R. H. Parmenter. "Isospin formulation of the theory of a granular superconductor". In: *Physical Review* 154.2 (1967), pp. 353–368. ISSN: 0031899X. DOI: `10.1103/PhysRev.154.353`.

[29] G. Deutscher et al. "Granular Superconducting Films". In: *Journal of Vacuum Science and Technology* 10.5 (1973), pp. 697–701. ISSN: 0022-5355. DOI: `10.1116/1.1318416`. URL: `http://avs.scitation.org/doi/10.1116/1.1318416`.

[30] N. Maleeva et al. "Circuit Quantum Electrodynamics of Granular Aluminum Resonators". In: (2018), pp. 1–17. arXiv: `1802.01859`. URL: `http://arxiv.org/abs/1802.01859`.

[31] Anton Bespalov et al. "Theoretical Model to Explain Excess of Quasiparticles in Superconductors". In: *Physical Review Letters* 117.11 (2016), pp. 1–5. ISSN: 10797114. DOI: `10.1103/PhysRevLett.117.117002`. arXiv: `1603.04273`.

[32] G. Calusine et al. "Analysis and mitigation of interface losses in trenched superconducting coplanar waveguide resonators". In: *Applied Physics Letters* 112.6 (2018). ISSN: 00036951. DOI: `10.1063/1.5006888`. arXiv: `1709.10015`.

[33] S. E. De Graaf et al. "Magnetic field resilient superconducting fractal resonators for coupling to free spins". In: *Journal of Applied Physics* 112.12 (2012). ISSN: 00218979. DOI: `10.1063/1.4769208`.

[34] C. Wang et al. "Surface participation and dielectric loss in superconducting qubits". In: *Applied Physics Letters* 107.16 (2015). ISSN: 00036951. DOI: `10.1063/1.4934486`. arXiv: `1509.01854`.

[35] Francesco Valenti et al. "Interplay between critical current density and nonlinearity in microwave kinetic inductance detectors". In: *In Preparation* (2018), pp. 1–6.

[36] H. Rotzinger et al. "Aluminium-oxide wires for superconducting high kinetic inductance circuits". In: *Superconductor Science and Technology* 30.2 (2017), pp. 1–16. ISSN: 13616668. DOI: `10.1088/0953-2048/30/2/025002`. arXiv: `1408.4347`.

[37] Lukas Grünhaupt et al. "Quasiparticle dynamics in granular aluminum close to the superconductor to insulator transition". In: (2018), pp. 1–13. arXiv: `1802.01858`. URL: `http://arxiv.org/abs/1802.01858`.

[38] You Peng Zhong et al. "Progress in superconducting qubits from the perspective of coherence and readout". In: *Chinese Physics B* 22.11 (2013). ISSN: 16741056. DOI: `10.1088/1674-1056/22/11/110313`.

[39] I. Nsanzineza and B. L.T. Plourde. "Trapping a single vortex and reducing quasiparticles in a superconducting resonator". In: *Physical Review Letters* 113.11 (2014), pp. 1–10. ISSN: 10797114. DOI: `10.1103/PhysRevLett.113.117002`. arXiv: `arXiv:1405.0256v1`.

[40] *Matter and Methods at Low Temperatures*. Springer-Verlag Berlin Heidelberg, 1992.

[41] M Martinez et al. "Measurements and simulations of athermal phonon transmission from silicon absorbers to aluminium sensors". In: (), pp. 1–10. arXiv: `arXiv:1805.02495v1`.